Inducing ferroelectricity and multiferroicity in undoped and doped BiFeO$_3$ -embedded Ti$_3$C$_2$T$_X$ MXene free-standing film

Khadeeja Kabir

Fall-2021-MS Physics

Reg No: 00000365194

Following thesis is submitted to fulfill the requirement of degree of **Master of Sciences**

In

Physics

Supervised by:

Prof. Dr. Syed Rizwan Hussain

Department of Physics

School of Natural Science (SNS)

National University of Sciences and Technology (NUST)

H-12, Islamabad, Pakistan

Year 2023

THESIS ACCEPTANCE CERTIFICATE

Certified that final copy of MS thesis written by **Khadeeja Kabir** (Registration No. **00000365194)**, of **School of Natural Sciences** has been vetted by undersigned, found complete in all respects as per NUST statutes/regulations, is free of plagiarism, errors, and mistakes and is accepted as partial fulfillment for award of MS/M.Phil degree. It is further certified that necessary amendments as pointed out by GEC members and external examiner of the scholar have also been incorporated in the said thesis.

Signature: _____

Name of Supervisor: Prof. Syed Rizwan Hussain

Date: 09-10-2023

Signature (HoD): _____

Date: 09-10-2023

Signature (Dean/Principal): _____

Date: 10-10-2023

ii

National University of Sciences & Technology

MS THESIS WORK

We hereby recommend that the dissertation prepared under our supervision by: Khadeeja Kabir, Regn No. 00000365194 Titled: Inducing Ferroelectricity and Multiferroicity in Undoped and Doped $BiFeO_3$ -Embedded Ti_3C_2TX MXene free-Standing Film be Accepted in partial fulfillment of the requirements for the award of **MS** degree.

Examination Committee Members

1. Name: DR. FAHEEM AMIN   Signature:_____

2. Name: DR. GHULAM ALI   Signature:_____

Supervisor's Name PROF. SYED RIZWAN HUSSAIN   Signature:_____

_____
Head of Department

05, 10-2023
_____
Date

COUNTERSINGED

Date: 10/10/2023

_____
Dean/Principal

This thesis is dedicated with heartfelt gratitude to my husband Mr. Arslan Ishaq, his unwavering support has been my rock throughout this journey.

Acknowledgement

Abstract:

This work reports emergence of ferroelectricity and multiferroicity in $Ti_3C_2T_x$ MXene free-standing film after introduction of $BiFeO_3$ (BFO), Z_{12} and Z_{13} nanoparticles at room-temperature. The nanoparticles and $Ti_3C_2T_x$ MXene ink were separately synthesized, followed by dispersion of nanoparticles in MXene ink. Structural and optical analysis was performed using X-ray diffraction (XRD) and Raman spectroscopy, respectively. The introduction of BFO (Bismuth Ferrite) and BFO-doped nanoparticles into the layered structure of $Ti_3C_2T_x$ resulted in distinct polarization versus electric field measurements. These measurements revealed previously unseen ferroelectric and multiferroic behavior in the MXene film, which was not observed in its pristine state. Furthermore, after subjecting the intercalated MXene to heat treatment, we observed enhanced ferroelectric characteristics. This enhancement can be attributed to the oxidation process affecting the $Ti_3C_2T_x$ MXene. It's worth noting that the highly reactive titanium atoms within the $Ti_3C_2T_x$ MXene play a pivotal role in generating crystalline TiO_2. It's crucial to emphasize that the oxidation of the prepared films is not complete, resulting in the coexistence of unreacted MXene within the core and oxide particles on the surface. The incorporation of BFO into the intercalated MXene has brought about multiferroic behavior, owing to the ferromagnetic characteristics exhibited by BFO. Contrary to our previous report on ferroelectricity induced only after heat treatment in $Ti_3C_2T_x$ MXene film. Here, we presented an alternate route to induce ferroelectricity and multiferroicity in MXene that will be useful for future data storage applications.

Table of Contents

Table of figures

Chapter 1: Introduction

1.1 Ferroelectrics:

More than a hundred years ago, the discovery of unusually high piezoelectric constants in a substance known as Rochelle salt served as a catalyst for the scientific investigation of ferroelectric materials. In the 1930s, researchers developed a theory explaining the ferroelectric phase transition when they observed that another group of materials, specifically those based on KH_2PO_4, exhibited ferroelectric properties. In the 1940s, scientists identified $BaTiO_3$ and related oxides with a perovskite crystal structure as ferroelectric materials, igniting further exploration into the recognition and characterization of such materials.[1]. A material is considered ferroelectric in a formal sense when it undergoes a phase transition. Initially, at high temperatures, it behaves like a regular dielectric, responding to an applied electric field by developing an electric polarization that disappears when the field is removed. However, as the temperature decreases to a lower phase, it exhibits spontaneous polarization that can be altered in direction by applying an external electric field. Structural deformation to a lower-symmetry phase occurs below the Curie temperature (Tc), instigating spontaneous polarization in crystal. A ferroelectric substance must be an insulator otherwise, an applied electric field would cause an electric current to flow instead of electrical polarization.

Polar and non-centrosymmetric crystal structures give rise to ferroelectricity in crystalline and polycrystalline materials. Spontaneous polarization (P_s) in non-centrosymmetric structure arises due to non-coinciding positive and negative charges resulting in ionic displacement. Anion and cation relative displacement within a unit cell retains even in absence of electric field known as remanent polarization. This remanent polarization can be reversed if electric field with opposite polarity is applied. Unlike ferroelectrics in linear dielectrics net polarization resulting from electron cloud and atomic nuclei distortion disappears on eliminating electric field[2]. Generally, polarization can be defined as a dipole moment per unit volume. It arises from redistribution or alignment of electric charges within the material. Polarization can be defined by equation[3]

$$P = \Sigma\ q_n r_n \qquad\qquad\qquad 0.1$$

q_n and r_n represent the charge and position vector of charge respectively. Net dipole moment of non-polar system is zero in the absence of external electric field while polar or ferroelectric

materials will yield a net dipole moment. Electric field displacement in free space can be given as [4]

$$D = \varepsilon_o E + P \qquad\qquad 0.2$$

Polarization can be written as

$$P = \varepsilon_o \chi_e E \qquad\qquad 0.3$$

χ_e is the materials electric susceptibility. Putting the polarization value in equation 1.2 electric field displacement becomes

$$D = \varepsilon_o E + \varepsilon_o \chi_e E = \varepsilon_o E (1 + \chi_e) = \varepsilon E \qquad\qquad 0.4$$

Where ε is material's permittivity. From equation 1.4 it can be written

$$\varepsilon_{r=} \frac{\varepsilon}{\varepsilon_o} = 1 + \chi_e \qquad\qquad 0.5$$

Introduction of electric field in ferroelectrics displaces ions inside non centrosymmetric crystal causing a net dipole moment known as spontaneous polarization. Equation 1.4 can be rewritten for ferroelectric.

$$D = \varepsilon_o E + \varepsilon_o \chi_e E + P_s = \varepsilon E \qquad\qquad 0.6$$

Spontaneous polarization term as result of ferroelectric dipole switching as well as non-switching dielectric term both are included in electric field displacement for ferroelectrics.

1.1.1: Theory behind Ferroelectricity:

A lattice comprising point charges with opposite polarities is fundamentally unstable because of the repulsive forces between closely situated electron clouds. Nevertheless, ionic materials manage to remain stable precisely because of these short-range repulsions among the adjacent charged entities. The interplay between the short-range repulsive forces, which tend to favor a non-ferroelectric symmetrical structure, and additional bonding factors, which could potentially

support the existence of the ferroelectric phase, must be carefully balanced in order to determine the presence or absence of ferroelectricity. At high temperatures, short-range repulsions
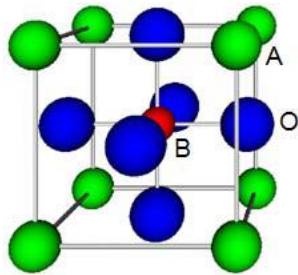
Figure 2: Structure of Perovskite oxide [5]
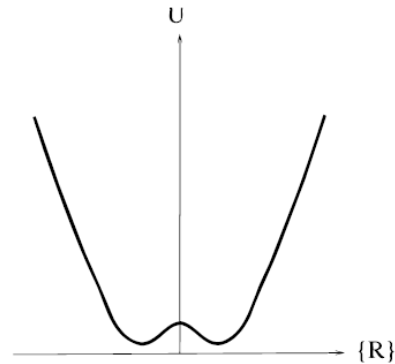
Figure 2: The distinctive double-well potential energy observed in perovskite ferroelectrics can be represented graphically as a function of the B cation's position between the oxygen anions [6].

predominate in ferroelectric materials as well, leading to the symmetric, unpolarized state.

Perovskite-structure oxides ABO_3 have been the most studied ferroelectrics. ABO_3 consists of O oxygen anions at octahedral positions and sizable cation located at the corners of the unit cell, with a smaller cation positioned at the center of the octahedron formed by oxygen anions. Fig. **1[5]**. In ferroelectric perovskite oxides, it is typically anticipated that the small B cation can effectively decrease its energy by moving along one of the [111] directions, unless there is lattice tension that favors a different displacement. Consequently, the position of the small cation between the oxygen anions in perovskite ferroelectrics demonstrates a unique "double-well" potential energy profile Fig. **2[6]**. The displacement of the B cation is only sustainable at lower temperatures. When the B cation is pushed beyond the Curie temperature, there is a restorative force that strives to return it to the center. The "soft mode" phonon, which is connected to this restoring force as the temperature drops, weakens until it reaches the Curie temperature, where the frequency is zero and the displacement happens on its own[6].

Ferroelectricity is produced by stereochemically active lone pair cations, such as Bi^{3+} or Pb^{2+} in $BiFeO_3$ or $PbVO_3$. The two electrons in the 5s or 6s orbitals of these divalent ions do not engage in chemical bonding. Local inversion symmetry is typically broken by cations that have a pair of valence electrons in the 5s or 6s state. The tiny B cation reduces its energy by moving in one of the [111] directions[5]. This structural alteration leads to a "double-well" shaped potential energy

describing the position of the tiny cation as a function of the separation between the oxygen anions in the system. Similarly, in BaTiO$_3$ the ferroelectric distortion must be stabilized by the Ti 3d-O 2p hybridization[6]. The Ba-O interaction in BaTiO3 is primarily ionic in nature.

1.2: Ferromagnetism and anti-ferromagnetism:

Below a specific phase transition, ferromagnetic materials change from a high-temperature paramagnetic phase to a low-temperature structure that has a spontaneous, nonvolatile magnetism. Magnetism arises from the presence of localized electrons within the partially filled d or f orbitals of transition metal or rare earth ions. These electrons each have a magnetic moment. So magnetic ordering results from exchange interactions between localized moments. Long-range ordering can be observed in ferromagnetic materials which causes unpaired electron spins to align parallel to one another in an area known as a domain.
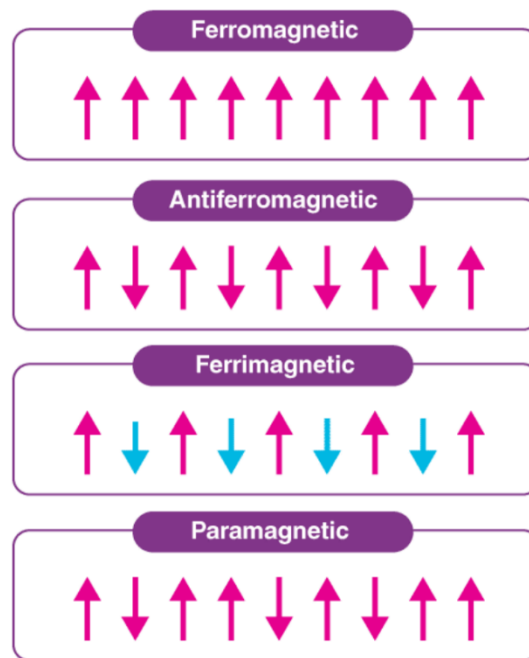
Figure 3 Magnetic ordering source google.

The Curie-Weiss localized-moment theory and the Stoner band theory of ferromagnetism are two theoretical frameworks for understanding various properties exhibited by ferromagnetic materials. Weiss' hypothesis states that electrons are regionalized and occupy specific energy levels. An electron's angular momentum affects its energy. Weiss proposed that in ferromagnetic materials, a "molecular field" from within aligns the magnetic moments so that they are parallel to one

another. The quantum mechanical exchange energy, which results in parallel spin electrons (and hence parallel magnetic moments) having a lower energy than antiparallel spin electrons with all other things being equal, is thought to be the source of this molecular field. The molecular field is sufficiently strong below the Curie temperature, Tc, that it magnetizes the substance even in the absence of an externally imposed field. When temperatures are high enough, the thermal energy, kT, exceeds the molecular field's alignment energy, causing the magnetic moments to have random orientations and exhibit paramagnetic behavior[7]. As per the Stoner theory, electrons have the freedom to move within a periodic potential. If each electron has the same spin, the exchange energy is reduced.

The spins of electrons in antiferromagnetic materials lack any overall macroscopic magnetization. These materials can go from a paramagnetic state to an antiferromagnetic ordering that is a low-temperature state. Multiple states with various energies can arise because of antiferromagnetic interactions. Antiferromagnetic materials can have a wide variety of spin configurations, including complicated spatial arrangements and regular patterns with adjacent spins pointing in opposite directions with no net moment[5].

1.3: Multiferroics:
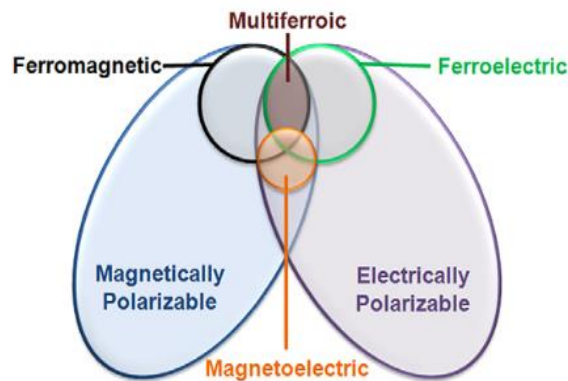
Figure 4 Multiferroics [8]

Materials with two or all three of the ferroelectricity, ferromagnetism, and ferro elasticity characteristics present in the same phase are referred to as multiferroics Fig. **4[8]**. This implies that these materials possess inherent magnetization, polarization, and deformation tendencies that can

be altered by the application of external magnetic fields, electric fields, or mechanical stress respectively[9].

1.3.1: Magnetoelectric Multiferroics:

A material must be both ferromagnetic and ferroelectric in order be considered as a magnetoelectric multiferroic[10]. Magnetoelectric multiferroics can be divided into two groups. One having independently generating ferroelectricity and magnetism and the second having ferroelectricity due to magnetism. The latter, however, exhibits significantly less polarization than the former because the spin orbit interaction, which is inherently weak, is often responsible for the polarization of magnetically induced ferroelectrics[11, 12].

Magnetoelectric multiferroics should have both properties ferroelectricity and magnetism. Magnetism requires partially filled d shells as opposed to ferroelectricity, which typically requires transition metal ions with empty d shells[13]. This explains why multiferroics are so hard to come
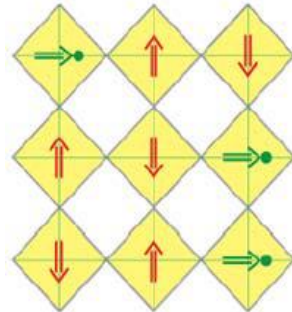
Figure 5 Shifts of d^0 ions from cores of O6 octahedra (yellow plaquettes) lead to polarization (green arrows), which coexists with magnetic order (red arrows) in "mixed" perovskites with ferroelectrically active d^0 ions (green circles) and magnetic d^n ions (red) [14]

by. A way to solve this issue is making "mixed" perovskites with both d^0 and d^n ions Fig. **5[14]**. Although there is still a weak link between magnetism and ferroelectricity in such mixed systems. For example, ferroelectricity is observed $BiMnO_3$ having magnetic Mn^{+3}. This is feasible because in this situation, different ions are linked to the ferroelectric and magnetic orders.

1.4: Applications:

Ferroelectrics and multiferroics have opened up new avenues for various applications. One notable advantage is the added versatility in device design, as they can couple with either electric or

magnetic polarization. Additionally, they are employed in multiple-state memory components, where data is stored using both electric and magnetic polarizations. These applications may also introduce innovative memory media, enabling the writing of ferroelectric data bits and the reading of the magnetic fields generated by their associations.[15].

Chapter 2: Literature Review

2.1: Nanomaterials and their classification

The fundamental of nanoscience and nanotechnology are nanomaterials. Nanomaterials should have at least one exterior dimension of 100 nanometers (nm) or less. At nanometer scale materials optical, electrical, magnetic and many other properties are changed. Nanomaterials are used in a variety of fields, including electronics and medicine because of their newly emerging features.

Nanomaterials can be categorized based on their dimensions, falling into the classifications of zero-dimensional (0D), one-dimensional (1D), two-dimensional (2D), and three-dimensional (3D), as depicted in Figure 6[16]. Zero-dimensional (0D) nanomaterials are those where all dimensions are confined within the nanoscale range, as exemplified by quantum dots.Fig. **6[16]**. 0D nanomaterials are materials having all dimensions within nanoscale like quantum dots. 1D materials have two dimensions confined within nanoscale such as nanowires[17]. 2D nanomaterials are materials having at least one dimension within 1nm to 100nm. Examples of 2D
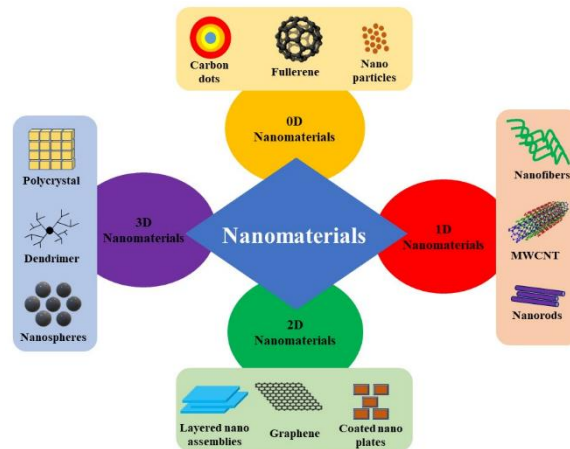
Figure 6 Nanomaterials classification [16]

include nano films and nanotubes. 3D materials commonly known as bulk materials have all three dimensions in macro scale. Examples of these structures include multilayer structures and polycrystalline structures[18].

This thesis focuses on 2D nanomaterials and their ferroelectric and multiferroic behavior.

2.1.1: Two Dimensional (2D) Materials:

2D materials have sheet like structure with at least two of its physical dimensions outside the range of nanomaterials [19]. K. S. **Novoselov et al**. reported the discovery of the first 2D structure

known as Graphene to be stable under ambient conditions in 2004[20]. It became a hot topic in material science and engineering. As it sparked the development of low dimensional materials with unusual physical and chemical properties displaying distinct features relative to their bulk. Due to the extremely high surface-to-volume ratio of 2D materials have wide variety of characteristics that would be otherwise unattainable. Researchers are now concentrating on 2D materials and several 2D materials other than graphene such as transition metal dichalcogenides (TMDs), phosphene and hexa-boron nitrate etc. are currently being explored to advance analysis.

2.2: MAX Phase:

The huge family of hexagonally layered ternary carbides/nitrides is known as MAX phase. Even till now new MAX phases been discovered and reported by scientific community. MAX phases exhibit a distinctive hexagonal crystalline arrangement characterized by the P63/mmc space group. MAX phase has a general formula of Mn AXn-1. Where M is a metal element mainly from the transition metals, A is element from group A. and X can be Nitrogen, carbon, or both at the same time in case of Carbonitride MAX. The crystal lattice of MAX phases is formed around the M6X octahedral site, with layers of elements spanning from groups IIIA to VIA positioned in between these sites. **Fig.8[21]** shows the periodic table with elements used to successfully synthesized MAX phases.

Within this structure, robust covalently bonded atomic layers of $M_{n+1}X_n$ are interspersed by A layers held together by less strong metallic bonds. This unique configuration grants MAX phases exceptional resistance to oxidation, as well as remarkable electrical and thermal conductivity properties.

Since the discovery of first MAX phase Ti_3SiC_2 by **M.W. Barsoum et al [22]**, in 1967, there was no work done on the removal of ceramic portion of MAX phase material to metallic or

semiconducting MXenes. In 2011, **Gogotsi et al. [23]** in their publications reported a new class

for 2D nanomaterials that can be synthesized by the process of chemical etching of already known
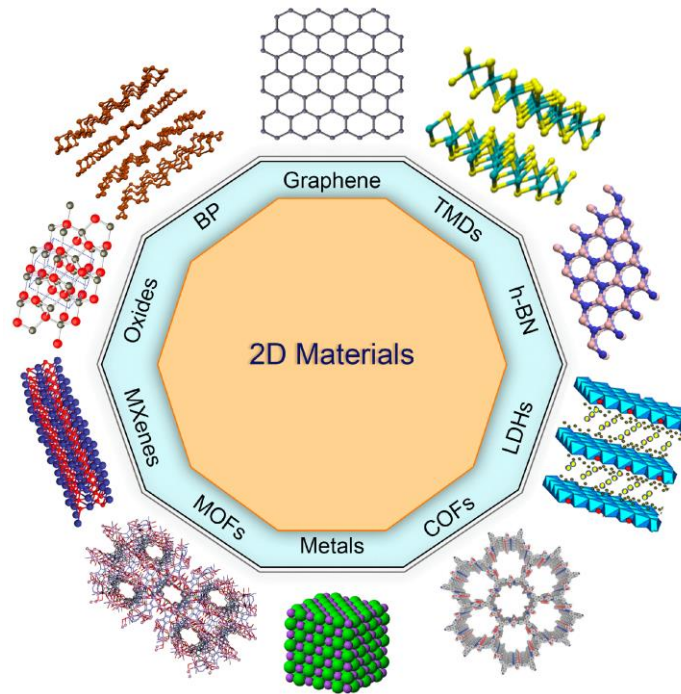
bulk materials MAX, they named its new class of materials as MXene. Where M is transition

metal, A is the group A element, and X can be carbon and nitrogen or both. As MXenes are a relatively new field of study so there are vast areas of application yet to be discovered.

2.2.1 MXene Phase:

MXenes are derived from a bulk crystal known as MAX. MXenes is a new category of transition metal nitrides, carbonitrides, and carbides in two dimensions (2D). Those 2D layered materials are known as "MXenes" because they are created by etching an A layer from MAX phases, and the suffix "ene" was added to emphasize how much they resemble graphene.

The structure of MXene is hexagonally closed packed crystalline form. MXenes are characterized by their generic formula $M_{n+1}X_nT_x$. In this formula, n typically ranges from 1 to 3, M represents a transition metal, and Tx denotes terminal groups introduced during the synthesis, which often include hydroxyl (OH), fluorine (F), and/or oxygen (O) groups[24]. Its M atoms are placed in a hexagon-like structure, and the X atoms are filled at the octahedral form. Because of their outstanding hydrophilicity, biocompatibility, high surface area, ease of post surface modification, and abundance of abundant elements (like Ti, C, and N), MXenes offer a wide range of applications.

Ti_3C_2 was the first member of MXene family which was successfully etched from their parent Ti_3AlC_2 MAX phase[25]. Till date extensive research on various synthesis routes has been made and twenty-two compounds of MXene have been reported so far[26]. Since MAX has a strong M-A bond it can tolerate any mechanical stress or shear and prevent itself from cleavage. The only remedy to synthesize MXene from their respective counter parts is through selective etching of "A" layer by some chemical reactions.

All the properties of the MAX phase materials are due to layered structure. The bonding between M-X is covalent in nature whereas M-A bonding is relatively weaker and subjected to strong acid like HF, these A-layered elements bond with fluoride ion of the acid to make salt. Because of its nature, MAX has a lot of practical applications, such as protective coating, high temperature thermally stable material and been used in electrical contacts.

The extraordinary characteristics of MAX phases stem from their layered structure and the unique combination of strong M-X bonds, which exhibit mixed metallic and covalent characteristics, along with relatively weaker M-A bonds. This distinctive blend of properties has led to extensive exploration of MAX phases for various applications, including but not limited to high-temperature

structural uses, protective coatings, sensors, electrical contacts, microelectromechanical systems, and numerous other fields.[27].

2.2.1.1 Chemical reactions:

During wet chemical etching using HF as etchant following reaction takes place.

$$M_{n+1}AX_n + 3HF \rightarrow M_{n+1}X_n + AF_3 + 1/2H_2 \qquad 2.1$$

$$M_{n+1}X_n + 2H_2O \rightarrow M_{n+1}X_n(OH)_2 + H_2 \qquad 2.2$$

$$M_{n+1}X_n + 2HF \rightarrow M_{n+1}X_nF_2 + H_2 \qquad 2.3$$
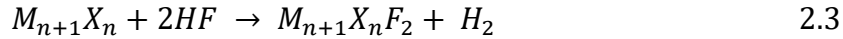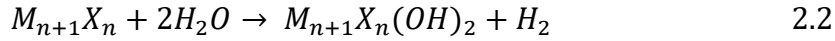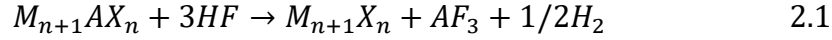
According to these equations, an element of the MAX phase reacts with F of the HF, yielding $M_{n+1}X_n$, which is then promoted to react with HF and H2O to provide surface functional groups[28]. Due to these functional groups, formula for MXene is generally written as $M_{n+1}X_nT_x$ [29].

Here, Tx denotes the surface terminations. The AlF$_3$ in these reactions can be Here Tx symbolizes the surface terminations. The AlF$_3$ in these reactions can be removed through several washings with the DI water until pH becomes neutral.

The factors that affect the synthesis of MXene are:

1. Etching time

2. Particle sizes of respective MAX phase powder

3. Concentration of HF.

4. Temperature

According to the researchers, the variety in M and A elements and the binding energies between M-Al bond changes, affecting the etching condition directly. These factors are used to increase the yield, reduce etching time, and improve the quality of MXene. According to the researchers, the variety in M and A elements and the binding energies between M-Al bond changes, affecting the etching condition directly. These factors are used to increase the yield, reduce etching time, and improve the quality of MXene.

2.2.2 MXene Delamination:

The process of delamination, which involves the complete detachment of individual layers from a layered structure, has been effectively achieved for single-layer flakes derived from layered materials through a variety of methods. These techniques include mechanical cleavage, chemical intercalation and exfoliation, as well as liquid exfoliation, among others[30, 31]. Similarly, several approaches have been documented in recent years for synthesizing single or few-layer flakes of

MXenes. The process of separating individual single or few-layer flakes from Multilayer (ML)-MXene particles can be quite challenging due to the strong interlayer interactions present within ML-MXene structures. Moreover, traditional etching methods for certain MXenes may not fully remove all bonded A layer elements between the M-X layers, making it difficult to achieve delamination using straightforward techniques. As a result, achieving the delamination of ML-MXenes into single or few-layer flakes typically requires an additional step, often involving a liquid-based delamination approach. This supplementary step is aimed at expanding the interlayer space and weakening interlayer interactions by introducing chemical intercalation with large organic or inorganic molecules between the MXene layers. Essentially, the intercalation of these larger molecules and ionic species leads to an increased interlayer spacing and a reduction in the out-of-plane interactions between stacked MXene layers[32]. This process is usually accompanied by significant swelling of the MXene powders due to the co-intercalation of water molecules.
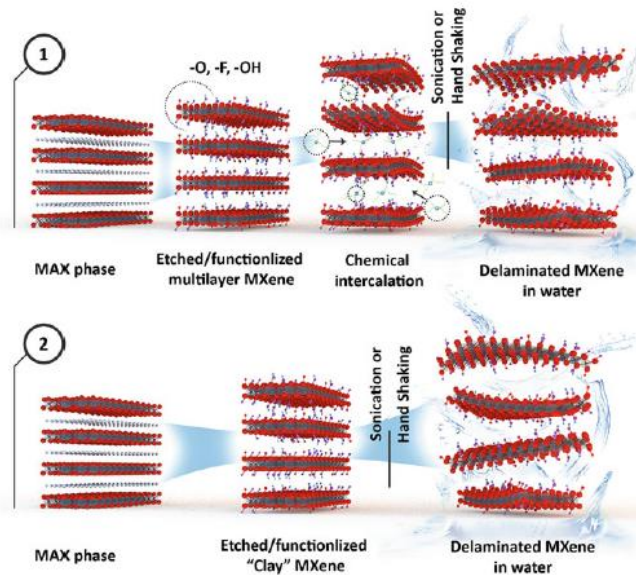
Figure 9 (1) The delamination process involves two steps. After the initial etching procedure, the ML-MXenes are exposed to intercalation with substantial organic molecules, followed by delamination through agitation methods like sonication or handshaking. Technique (2) is suited for MXenes that can undergo etching within a combination of metal salts and acids. This method serves as a single-step approach encompassing both etching and delamination [35].

It's worth noting that $Ti_3C_2T_x$, a well-researched MXene, has been extensively investigated in terms of synthesis, exfoliation, delamination methods, and potential applications. The term "T_x" in the MXene formula denotes the functional groups terminating the material's surface. The notable increase in the interlayer spacing (c-LP) weakens the interaction between M-X layers. When interlayer-expanded ML-$Ti_3C_2T_x$ is subjected to sonication in water, this leads to the delamination of single or few-layer MXene flakes[33]. For various other MXene compositions, a two-step etching, and delamination process has been successfully used, employing different intercalants. In 2014, Ghidiu et al. introduced an efficient one-step method for synthesizing $Ti_3C_2T_x$. In thismethod, a solution containing lithium fluoride (or other fluoride salts) and hydrochloric acid is utilized as the etchant, in contrast to concentrated HF solutions[34]. During the etching process, aluminum atoms are removed from Ti_3AlC_2, and simultaneously, hydrated Li ions are intercalated between the M-X layers, resulting in the delamination of single or few-layer $Ti_3C_2T_x$ flakes. as in Fig. 9[35].

2.2.3 Properties of MXene

MXene has loads of remarkable properties far superior to graphene. The MXene materials are thermally conductive, higher melting points, large surface areas, hydrophilic surfaces, and along with that it can intercalate or delaminate many ions[36] At the time of discovery of MXene, its electronic properties and structure were undiscovered and unidentified because different surface termination group were attached due to reactivity of bear MXenes. The surface termination groups of MXene also affect the band gap of the MXene materials. The same MXene material can be a metal with one Tx group and can be a semiconductor material with another Tx site. Based on which bandgap increases or decreases along with that it can change direct bandgap into indirect bandgap and vice versa. This all is relying upon the electron density of states near Fermi level. **Naguib et al.** in his first paper on MXene elaborated that Pristine Ti3C2 MXene is pure metallic but if surface terminations attached that is Ti3C2(OH)₂ and Ti2C3F2, the band gap rises to 0.05eV and 0.1eV. MXenes electrical conductivity is also dependent upon the method of synthesizing compounds. Flakes with large sizes, better contact between each of the flakes, sonication free delamination, optimized temperature, and environment, drying and defect free surface concludes comparably higher ranges of conductivity. The conductivity ranges are from 1000S/cm to 6500S/cm[37, 38]. The single flake of MXene sheet is unstable in the oxygen environment or exposure to light and water but it is quite stable in oxygen free environment and dry air. The oxidation process is

increased when exposure to light increases, and it is generally initiated with the edges and forms metal oxide with the surface termination sites. In general, Pristine MXene flakes are very much stable and depend upon synthesizing processes[39]. MXene materials at higher temperatures are still emerging, as it is also dependent on the kind of MXene and nanocomposite of it. For example, Ti3C2Tx is stable in argon atmosphere at 773 Kelvin nonetheless TiO2 particles formation occurs at the ends. Ti3C2 structure is also preserved at a temperature 1473K in an argon atmosphere but at higher temperatures the annealing processes occurred [40, 41].

2.2.4 Practical Applications of MXene

The MXene family is mounting with the passage of time due to the increase in its composites and crystallinity variation which results in diverse applications that is why MXenes 20 are considered as multifunctional materials owing to its tunable surface, large surface area depending upon the need of the application, varying termination groups adsorption capabilities, highly reactive surface and much more.
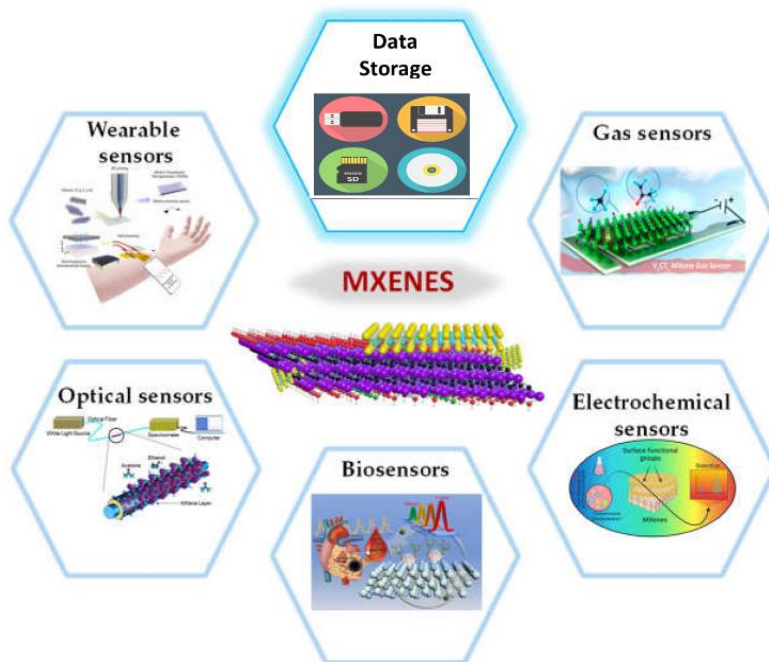
Figure 10 MXene Applications

2.3 Bismuth Ferrite BiFeO₃ (BFO):

During the late 1950s, researchers successfully synthesized the perovskite $BiFeO_3$ (BFO). It has been well-established that BFO possesses antiferromagnetic properties and exhibits multiferroic behavior as a ferroelectric material. In its bulk form, BFO demonstrates a ferroelectric Curie

(a) Perovskite Structure   (b) Rhombohedral distorted perovskite structure
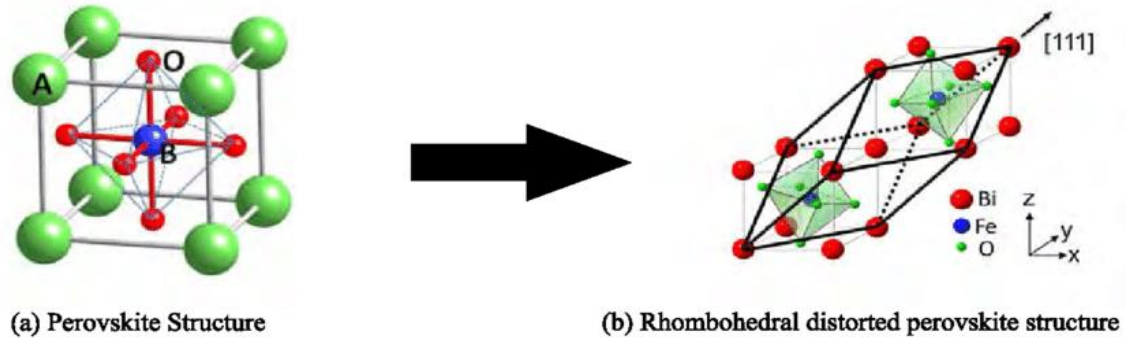
Figure 8 BFO rhombohedral distorted structure [42].

temperature of TC=1103°C. There are, however, relatively few single-phase multiferroic compounds in nature that exhibit (anti-) ferromagnetism and ferroelectricity concurrently at room temperature, among them BFO is the most well-known. A ferroelectric perovskite with the space group R3c that is rhombohedrally distorted Fig.[42] can be used to describe bulk bismuth ferrite. The emergence of spontaneous polarization (Ps) along the pseudocubic [111] direction is made possible by the R3c symmetry[5]. When a considerable ferroelectric polarization of about 60 C/cm2 was initially exhibited by BFO epitaxial thin films in 2003, it marked a significant breakthrough[43, 44]. In BFO-based thin films, the Pr value can be greater than 150 C/cm2 due to buffer layer effects, composition modification, and substrate or lattice strain[45, 46].   Because of its huge polarization expected, the super-tetragonal phase of BFO has more recently attracted scientific attention[47]. The massive Pr up to 230 C/cm248 was demonstrated in BFO-based thin films with super-tetragonal phase, which may be related to the large c/a ratio of 1.25[48, 49].

2.3.1 BFO magnetic behavior:

In accordance with the magnetic structure of BFO, it adopts a G-type antiferromagnetic configuration, as shown in Figure 10[8]. This magnetic structure is observed below a critical temperature, denoted as T_N, which is approximately 673 K. Furthermore, BFO exhibits a modified cycloidal spin structure characterized by a long periodicity spanning 62 nm. In this arrangement, each Fe+3 spin is encircled by six antiparallel spins originating from its closest Fe neighbors, thus forming a G-type antiferromagnetic pattern. This implies that the magnetic moments of Fe are antiferromagnetically coupled between adjacent planes while displaying ferromagnetic alignment within the pseudocubic (111) planes. As a consequence of ferroelectric switching, the antiferromagnetic order is expected to reorient, leading to the anticipation of intriguing
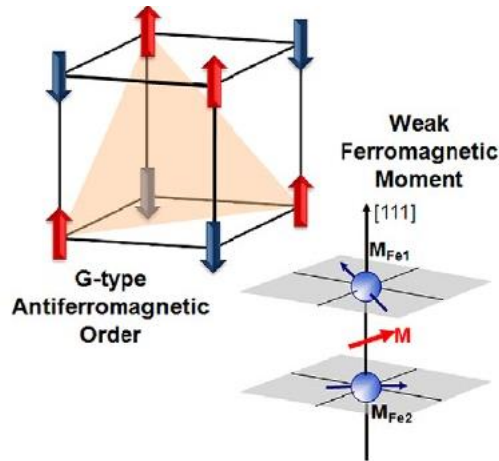
Figure 9 BFO magnetic behavior [8]

magnetoelectric switching characteristics in $BiFeO_3$ films. [50]. Some theories also claimed that the weak ferromagnetism caused the antiferromagnetic moments in BFO to tilt. The canting angle was determined to be 1 and would result in a weak magnetization of 0.05 B per unit cell. According to Dzyaloshinski-Moriya hypothesis, the domain walls of BFO might exhibit a weak ferromagnetic moment if the moments are aligned perpendicular to [111][51]. However, the validity of this notion has not yet been established[50].

2.3.2 BFO ferroelectric behavior:

Deeper exploration has revealed that the substantial displacement of ionic bismuth (Bi), triggered by the presence of stereochemically active 6s lone pairs, is the underlying reason behind the polarization phenomenon. This substantial Bi ion displacement results in the emergence of eight unique polarization directions, encompassing both positive and negative orientations, along the four cube diagonals (labeled as Pi with i=1,4). These directions correspond to four distinct structural variants. Fig. **9[5]**, are formed by the ferroelectric polarization of BFO along the 111>
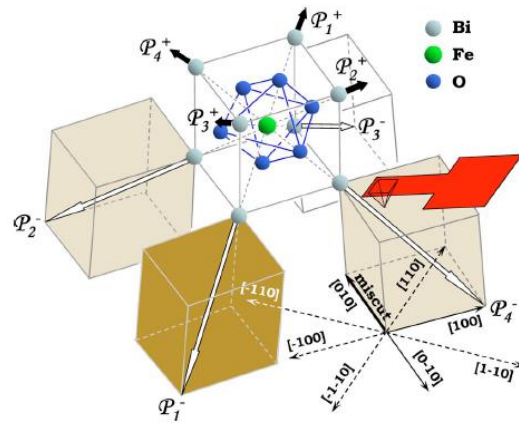
Figure 10: An illustration of the four distinct structural variations found in (001) rhombohedral films. The polarization vectors are denoted by pi with i=1,4. The central unit is a representation of the rhombohedral structure's perovskite building component [5].

direction.

2.3.3 Ion substitution

Enhancing the electrical characteristics of Bismuth Ferrite (BFO) ceramic materials are frequently pursued through ion substitution. This method involves replacing ions in either the bismuth or iron positions within the material's structure. Notably, substituting ions at the bismuth site can significantly alter the ferroelectric and piezoelectric properties, leading to a reduction in leakage current[52, 53]. The impacts of ion substitutions at various sites in BFO are elaborated upon below with comprehensive detail.

2.3.3.1 Bi substitution

Doping certain elements into the bismuth site of BFO ceramics has demonstrated the capability to influence its phase structure, as evident from various studies[54]. This doping-induced alteration in phase structure is accompanied by corresponding changes in the material's properties[55].

Specifically, when rare earth elements are introduced as dopants in BFO compounds, they induce a transition in the phase structure from its initial rhombohedral form to other configurations[56]. The specific nature and quantity of the intercalated rare-earth elements significantly impact the resulting phase structures.

2.3.3.2 Fe substitution:

Much like the substitution occurring at the bismuth site, replacing ions within the iron site of BFO ceramics also exerts an influence on the material's phase structure and relevant properties. However, in contrast to bismuth site substitutions, ion replacement at the iron site typically leads to diminished ferroelectric and piezoelectric performance[57]. Nonetheless, it is worth noting an enhancement in magnetic behavior in some instances[58]. The decline in electrical properties, specifically ferroelectric and piezoelectric behavior, might arise from the introduction of secondary phases induced by the dopants, such as Co, Nb, Sc, Zn, Zr, and Ni[59]. While certain magnetic elements introduced through doping can enhance the magnetic properties of BFO ceramics, achieving an optimal balance between magnetic and ferroelectric properties remains a challenge. While substitution with a suitable magnetic element at the Fe site can generally lead to improvements in magnetic behavior, striking the right compromise between magnetic and ferroelectric characteristics within BFO ceramics remains a complex task[60].

2.3.3.3 Bi and Fe co-substitution:

Numerous investigations have explored the utilization of diverse elements to concurrently substitute both bismuth and iron sites in BFO ceramic bulks. These studies delve into the impacts of such substitutions on the material's phase structure and various physical properties. In BFO, the ferroelectric characteristics are attributed to the presence of lone pair electrons in the Bi 6s orbital, while the magnetic properties stem from the partially occupied d orbitals of Fe[12, 61]. Consequently, strategic modifications in both the bismuth and iron sites through chemical substitutions hold the potential to enhance the material's electrical attributes (including ferroelectric and piezoelectric behavior) as well as its magnetic properties[62].

2.4 Ferroelectric and Multiferroic Behavior in materials:

2.4.1 Ferroelectric and Multiferroic Behavior in MXenes:

Rabia et al. The initial research report unveiled the discovery of ferroelectric and multiferroic properties in a Ti3C2Tx MXene film that underwent heat treatment, all occurring at room

temperature. The film exhibited substantial polarization values under an electric field and retained some polarization even when the field was removed. Additionally, magnetoelectric tests demonstrated a strong coupling effect within the film, with the ability to alter its polarization using an external magnetic field. These findings underscore the potential of MXene as a promising 2D material for future data storage device applications.[63].

Rabia et al. reported free-standing $Ti_3C_2T_x$ MXene film was produced and subsequently subjected to optimized heat treatment. To explore the presence of ferroelectric properties at room temperature, polarization vs. electric field (P-E) experiments across a range of frequencies were conducted. These experiments consistently revealed the characteristic behavior of ferroelectric materials, regardless of frequency. Additionally, the existence of magneto-electric coupling through the observation of asymmetric P-E loops when static magnetic fields were applied, complemented by measurements of the coupling between magnetic and electric properties[64].

Rabia et al. reported that in $Ti_3C_2T_x$ as the electric field increases, the electric domains align with the field, approaching saturation. Even when the electric field returns to zero, remanent polarization (P_r) is still evident, a characteristic of ferroelectric materials. Increasing the applied electric field from 2.5 to 5 kV/cm also increases the coercive field (E_c) and P_r. At lower fields like 2.5 kV/cm, the polarization loops are not fully closed, possibly due to back polarization switching, as domains aren't fully aligned. At higher fields, a uniform, closed ferroelectric hysteresis loop is observed when most domains align. Ferroelectricity in the $Ti_3C_2T_x$ MXene film is attributed to the formation of the TiO_2 phase, which can produce ferroelectricity under uniaxial strain, as supported by density functional theory calculations. Additionally, a slightly distorted ferroelectric behavior observed at a slightly higher annealing temperature of 150°C [65].

Chapter 3: Synthesis and Characterization techniques

In this chapter, a brief discussion is provided about the apparatus used throughout the experimental synthesis procedure of both MXenes and their composites. Afterwards all the necessary characterization techniques will be discussed. Which includes generalized discussion on XRD, SEM, EDX, Raman, Vibrating Sample Magnetometers (VSMs), Precision Multiferroic II (Precision Material Analyzer) etc. used to analyze structural elemental and ferroelectric properties of the material.

Apparatus used:

The following is the list of commonly used apparatus during the entire period of experimental research.

- Weight balance
- Teflon Beaker
- Hotplate
- Thermometer
- Glass beakers
- Fume hood
- Heavy-duty Gloves
- Centrifuge machine
- Vacuum Filtration Assembly
- 0.22um pore size Filter papers
- Vacuum Oven
- Bath and Probe Sonicator

Materials used in synthesis:

Following are the list of materials and chemicals used in the synthesis of MXene and their composites

- Hydrofluoric acid (48-50%)
- Deionized Water (DI)
- Hydrochloric acid (HCL) 12M
- Acetone
- Ethanol

- Acetic acid
- Ethylene Glycol
- MAX Powder
- BFO
- Z_{12}
- Z_{13}

3.1 Synthesis:

3.1.1 Ti_3C_2 T_X MXene etching:

To create $Ti_3C_2T_X$ MXene, a process was employed to specifically eliminate aluminum (Al) from commercial-grade Ti_3AlC_2 MAX powder. In a typical procedure, 1.0 gram of sifted Ti_3AlC_2 MAX phase was immersed in a solution containing Hydrofluoric acid (HF) with a concentration of no less than 48% (1 ml of HF from Sigma Aldrich), Deionized water (3 ml of H2O), and Hydrochloric acid (HCl) with a concentration of 37% (equivalent to 12M, 6 ml of HCl). This solution was mixed in a volume ratio of 1:3:6 while maintaining constant stirring for a duration of 24 hours in oil bath at 35ºC. The process began by gradually adding the Ti_3AlC_2 powder in small increments over a span of 5-8 minutes into a Teflon-lined reaction vessel, which was then sealed. Subsequently, the mixture was thoroughly rinsed with Deionized water multiple times, with each cycle involving the discarding of the supernatant to eliminate any undesirable adsorbed ions. The remaining sediment was dispersed in Deionized water until the solution reached a pH of 7. Finally, the etched powder was gathered through filtration and left to dry naturally overnight at room temperature.

3.1.2 $Ti_3C_2T_X$ Delamination (de-$Ti_3C_2T_X$):

The multilayer (ML) Ti3C2Tx MXene was exfoliated using lithium chloride (LiCl, 99%). First, the ML-MXene powder was dispersed in a 50 ml of 0.5M LiCl solution. The solution was continuously stirred overnight in an oil bath at 35ºC. Afterward, the resulting intercalated dispersion was subjected to centrifugation at 3500-4500 rpm for 10 minutes, and this centrifugation step was repeated until a stable MXene ink with a wet clay-like paste sediment was obtained.

Following each separation, additional deionized water (DI) was added to the sediment, which was then re-dispersed and subjected to centrifugation. This process was repeated until the desired MXene ink was achieved. The resulting ink was carefully transferred to a separate centrifuge tube

and centrifuged for 30 minutes at 3500 rpm to ensure the complete removal of any remaining ML powder. The supernatant MXene solution, which remained stable even after extended centrifugation, was subsequently vacuum filtered using Celguard membranes, and these membranes were then employed to produce free-standing films.

3.1.3 $BiFe_{(1-x)}Se_xO_3$ nanoparticles Synthesis:

$BiFe_{(1-x)}Se_xO_3$, x=0,0.25,0.75 namely $BiFeO_3$(BFO), $BiFe_{0.75}Se_{0.25}O_3(Z_{12})$, $BiFe_{0.5}Se_{0.5}O_3(Z_{13})$ were synthesized using double solvent sol-gel technique[66, 67].

3.1.4 $BFO@Ti_3C_2T_X$, $Z_{12}@Ti_3C_2\ T_X$ and $Z_{13}@Ti_3C_2\ T_X$ Free standing films synthesis:

A solvothermal technique was employed to synthesize free-standing films of $BFO@Ti_3C_2$ with a 50:50 doping ratio. Initially, 50 mg of BFO nanoparticles were dissolved in a mixture consisting of acetic acid and ethylene glycol in a 1:1 ratio, with a molarity of 0.01 M. This BFO solution underwent ultrasonication for 1 hour at 60°C. Subsequently, a De-Ti3C2 ink containing 50 mg of MXene, having the same concentration in mg/mL as that of prepared BFO solution, was introduced into the BFO solution. The mixture was continuously stirred in an oil bath at 80°C for 2 hours. The resulting product was thoroughly washed with deionized (DI) water multiple times until the ink is regained, after which it was dried at 80°C for 3 hours. Free-standing films of $Z_{12}@Ti_3C_2\ T_X$ and $Z_{13}@Ti_3C_2\ T_X$ with a 50:50 doping ratio were synthesized using the same procedure.

3.2: Characterization Techniques:

The next step after synthesizing the MXene ink and composites is to analyze their particle size, phase, structure, the functional groups, specific area of the surface, morphology, and composition.

- ➢ X-Ray Diffraction (XRD)
- ➢ Scanning Electron Microscopy (SEM)/ Energy Dispersive X-ray (EDX)
- ➢ Raman Spectroscopy (Raman)
- ➢ Vibrating Sample Magnetometers (VSMs)
- ➢ Precision Multiferroic II (Precision Material Analyzer)

3.2.1: X-ray Diffraction (XRD)

The main use of XRD analysis is to recognize materials established by their diffraction pattern. Moreover, apart from phase identification, XRD also gives data on how the real structure varies from the perfect structure, due to internal stresses and defects.

3.2.1.1: Working Principle:

When light waves of sufficiently small wavelength reach the lattice, they are diffracted from the points of the lattice. At specific incident angles, the bent parallel waves interfere with each other and generate peaks with intensity. Arrays of regular pattern refers to Crystals while electromagnetic radiation in the form of waves is referred to as X-rays. Through the interaction with atom's electron, incident x-rays are scattered by crystal atoms, resulting to a phenomenon called elastic diffusion. A evenly diffused array creates a normal spherical wave array. Through destructive interference, the waves in some direction cancel each other, and I some cases, they complement each other constructively in specific paths as defined by Bragg's Law Fig. 14[68]:

2 d sin θ = n λ

were,

d denotes the distance between the diffraction planes

θ represents the incidence angle

n is representing an integer

λ denotes wavelength of the beam.
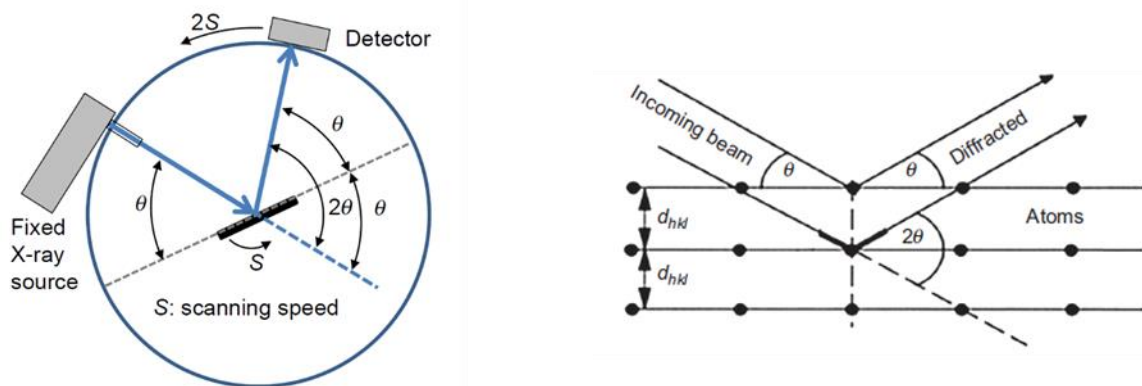
Figure 11 Condition for Bragg's law [68]

The exact directions that seem like points on the spreading pattern are termed reflections. Thus, XRD patterns are the consequence of electromagnetic rays hitting a well scattered array. Electromagnetic rays are utilized to generate diffraction images since they possess a wavelength (λ) that is approximately equal to the distance(**d**) between the crystal. Diffraction arises only when Bragg's law fulfills the requirement for generating interference of planes

with distance d.

3.2.1.2: Application:

XRD is a technique that does not destroy the sample and is primarily used to

1. Determine crystal orientation and phases of crystal or grain.

2. Define structural properties such as size of grain, parameters of the lattice, tension, and composition of phase.

3. Measure multi-layer and film thickness as well as the average distance between layers or rows of atoms.

4. Determine the atomic arrangement.

3.2.2 Scanning Electron Microscopy (SEM) and Energy Dispersive X-ray (EDX):

Through SEM, 2D image are produces by examining the surface of sample with a concentrated electron beam. Through the interaction of electrons and atoms in the sample, signals are produced that comprise information regarding the surface composition and topography of the sample.

3.2.2.1: Working principle:

Works on the principle of electron scattering at the sample surface. Electrons from the source/electron beam (primary electrons) are directed towards the sample surface in a raster sweep pattern. The electron transfers part of its energy to the sample, which is then emitted to the sample surface.

The excited electrons from the sample then produce signals in the form of backscattered electrons, secondary electrons (SE) and characteristic X-rays containing information about the sample. Multiple recorded SEs resulted in brighter points of the image being formed, some recorded SEs resulted in blurry or gray spots, and none resulted in dark spots. This is done row by row until the entire surface of the scanned sample forms a rectangular image

on the screen Fig.15[69].
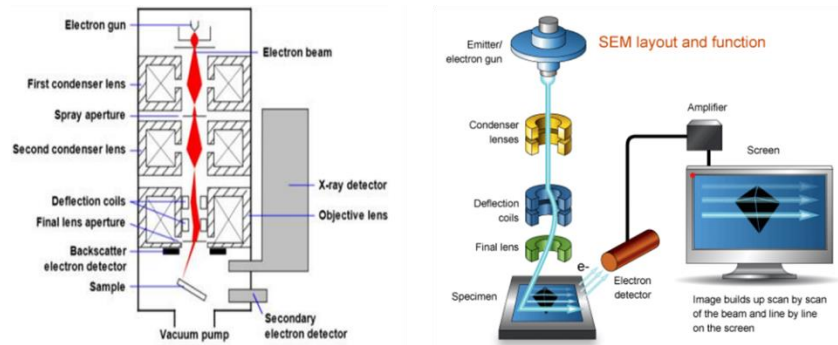
Figure 12 SEM illustration [69].

Energy Dispersive X-ray Spectroscopy- EDX

It's process of acquiring and characterizing X-rays to determine the chemical composition of a sample. When PE knocks electrons out of the atom's K shell, an empty spot remains, creating an unstable state. The outer shell electron falls to fill up the empty space, releasing a characteristic X-ray photon. X-ray energy is produced due to the difference in ionization energies of electrons during a transition and is specific to a particular element.

3.2.3 Raman Spectroscopy (Raman)

A non-destructive chemical analysis technique, Raman spectroscopy gives detail knowledge about crystallinity, chemical structure, molecular interactions and phase. Raman is employed to analyze a wide range of samples that includes solids, slurries, powders, liquids, gels, inorganic, metal oxides amongst others.

3.2.3.1 Working principle:

It is centered on the interaction of chemical bonds with light in the material. When monochromatic radiation reaches the sample surface, it can be scattered, absorbed, or reflected in one way or another. **Rayleigh scattering**, which comprises of about 90% of the scattering, has the same wavelength as the laser source, and gives no beneficial information. The remaining scattering
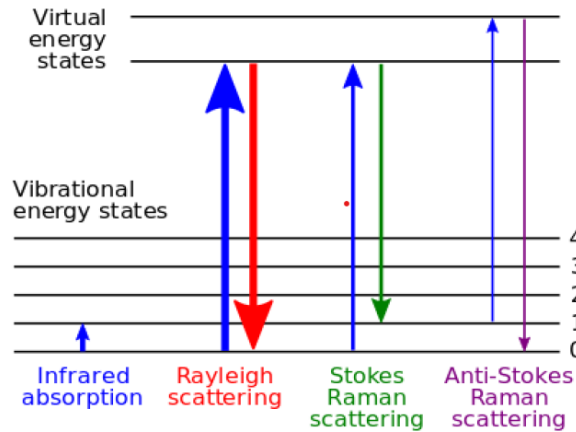
Figure 13 Schematic view of RAMAN effect [70]

constitutes **Raman scattering** and they have different wavelength to that of the laser source. Raman scattering is divided into **Stokes scattering** (energy of incident photon greater than that of the scattered photon) and **Anti-Stokes Raman scattering** (energy of incident photon less than that of the scattered photon). Raman spectrum (determined by plotting the intensity of this "shifted" light against the frequency that gives the sample's Raman spectrum) Fig.16[70].

3.2.4 Vibrating Sample Magnetometers (VSMs):

Vibrating sample magnetometers (VSMs) possess the ability to evaluate the magnetic characteristics of diverse materials, spanning from those exhibiting low coercivity (magnetically soft) to high coercivity (magnetically hard), in a broad spectrum of physical states, including solids, powders, single crystals, thin films, and liquids. They offer the flexibility to conduct measurements across a broad spectrum of magnetic field strengths, utilizing methods like electromagnets, Halbach rotating permanent magnet arrays, or high-field superconducting magnets. Moreover, VSMs are equipped to operate effectively across a vast temperature range, making use of integrated cryostats for low-temperature measurements and furnaces for high-temperature experiments. These instruments possess an extensive dynamic range, spanning from

10^-8 emu (equivalent to 10^-11 Am^2) to well above 10^3 emu (equivalent to 1 Am^2). This versatility enables them to characterize materials with magnetic properties that vary from very weak (such as ultrathin films and nanoscale structures) to exceptionally strong (like permanent magnets)[71].

3.2.4.1 Working principle:

The Vibrating Sample Magnetometer (VSM) operates based on Faraday's law, which states that when a conductor experiences a time-varying magnetic flux, it induces an electromotive force (e.m.f.). In the VSM, a sample is magnetized by a consistent magnetic field and then subjected to
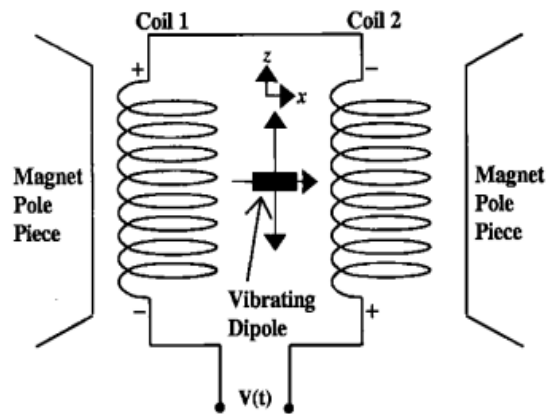
Figure 14 VSM working principle [72].

sinusoidal vibrations at a small, constant amplitude in the vicinity of stationary pick-up coils. The change in the magnetic field ($\partial B(t)$) at a specific point (r) within the detection coils leads to the generation of a voltage signal (B(t)). This process is approximated using the dipolar approximation, assuming that the dimensions of the magnetized sample are much smaller than its distance from the detection coils (m). To achieve high-resolution and accurate detection of V(t), specialized electronics are employed. When stationary pick-up coils are used in conjunction with a uniform and stable external magnetic field, the coils exclusively detect the effects caused by the sample's motion. Consequently, the voltage signal V(t) serves as a measurement of the magnetic moment of the sample Fig.17[72].

3.2.5 Precision Multiferroic II (Precision Material Analyzer):

Figure 15 Precision Multiferroic II (Precision Material Analyzer); Radiant Technologies Inc.

3.2.5.1 Hysteresis Task:

The Hysteresis Task is a widely used method for characterizing ferroelectric samples, offering users versatility in their measurements. In this task, a voltage waveform is systematically applied to the sample through incremental voltage steps. At each step, the resulting current induced in the sample is integrated, and this integrated value is then recorded and converted into Polarization ($\mu C/cm^2$). The Hysteresis Task provides a variety of predefined DRIVE port signal profiles for generating responses in Polarization ($\mu C/cm^2$), which are measured at the RETURN port. Measurement data for the Hysteresis Task includes recorded information on Polarization ($\mu C/cm^2$), Voltage, and Time (ms).

3.2.5.1.1 Standard bipolar (P-E Loops measurement):

The voltage waveform typically takes the shape of a standard bipolar triangular waveform. This waveform can be easily defined by specifying the maximum voltage and the total duration in milliseconds. The initial segment's direction depends on the polarity of the voltage. The number of data points in the waveform primarily depends on its duration, but the voltage setting can also have an impact. The software calculates the number of points automatically, providing the maximum possible number based on the specified conditions (details on point calculation are

discussed below). The waveform starts at 0.0 volts and then increases to reach the specified maximum voltage. It then descends to the negative equivalent of the given maximum voltage and returns to zero volts. If desired, a DC bias level can be applied, allowing the entire waveform to shift away from the zero-volt symmetry point while maintaining the waveform's symmetry. Regenerate. The standard bipolar waveform yields five key derived parameters:

- ❖ P_{Max}: This represents the polarization observed at the maximum applied voltage.
- ❖ $+P_r$: This indicates the polarization at zero volts when the voltage transitions from positive to negative. If V_{Max} is a negative value, this will denote the polarization at the final sample point.
- ❖ $-P_r$: This signifies the polarization at zero volts when the voltage transitions from negative to positive. If V_{Max} is a positive value, this will denote the polarization at the final sample points.
- ❖ $+V_c$: This denotes the voltage level at which polarization reaches zero when switching from negative to positive.
- ❖ $-V_c$: This signifies the voltage level at which polarization reaches zero when switching from positive to negative.

3.2.5.1.2 Double monopolar sine (stability test):

In the case of double monopolar sine, the voltage increment does not follow a linear pattern; instead, it follows a sinusoidal trajectory.

3.2.5.2 Leakage Task (Leakage current measurement):

The Leakage Task, categorized as a Vision Measurement Task, involves the continuous monitoring of the stable current passing through the test element, which is connected to the Precision tester. To achieve this, a constant DC bias voltage is applied to the sample. Prior to initiating the measurement, a user-defined delay period, often referred to as a "Soak" period, is introduced. This delay is designed to allow ample time for any polarization-switching current or other induced currents resulting from the voltage application to settle, ensuring that the sample reaches a steady state. Following this delay period, a measurement phase commences, during which the current flowing through the device under examination is consistently sampled and recorded.

3.2.5.3 Magneto-Electric Response task (dP /dH ME coupling coefficient measurement):

The Magneto-Electric Response Task is employed to quantify the charge produced by a ferroelectric or multiferroic specimen when subjected to a fluctuating magnetic field, generated using a Helmholtz coil. This task involves the generation of current by applying a voltage profile specified by the user, which is produced by the Precision tester and directed to the Radiant CS 2.5 Current Amplifier. The current amplifier subsequently delivers a variable current directly linked to the input voltage profile to the Helmholtz coil. This coil generates a variable magnetic field, proportionate to the input current, and applies it to the sample, inducing a charge response in the sample. The resulting charge is then measured at the tester's RETURN port.

3.2.5.4 P-V measurement under fixed Magnetic field:

To generate the DC magnetic field strength (measured in Gauss), you should employ the CS 2.5's DC Voltage/Magnetic Field Task. In this scenario, you will connect either the CS 2.5 Field Bias 1 or Field Bias 2 to the input of the amplifier, depending on the specific Task chosen. Once the Task is executed, the DC magnetic field will persist within the magnet until you run the Task again with
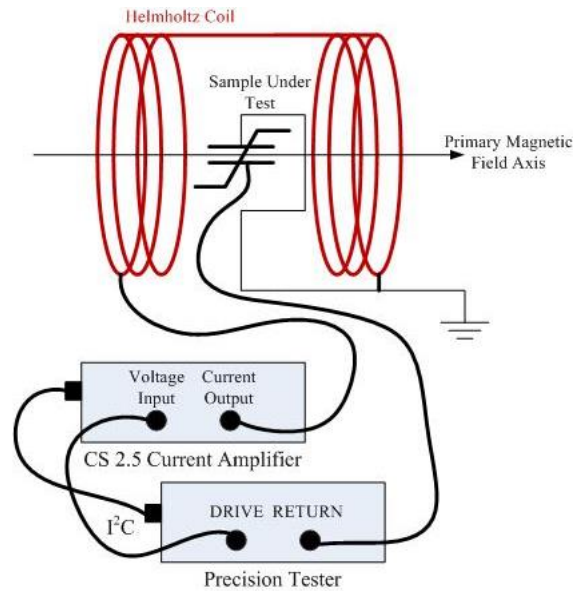

Figure 16 Magneto-electric task configuration

a different level, or until you decide to deactivate the CS 2.5 and/or the electromagnet amplifier.

Chapter 4: Results and discussion BFO@Ti$_3$C$_2$T$_X$

In order to analyze the as-prepare samples, various structural and ferroelectric and multiferroic characterizations were utilized.

4.1 X-Ray Diffraction (XRD):

To analyze the composition and crystal structure, a powder Xray diffractometer with a Cu K-$\alpha\lambda$ =
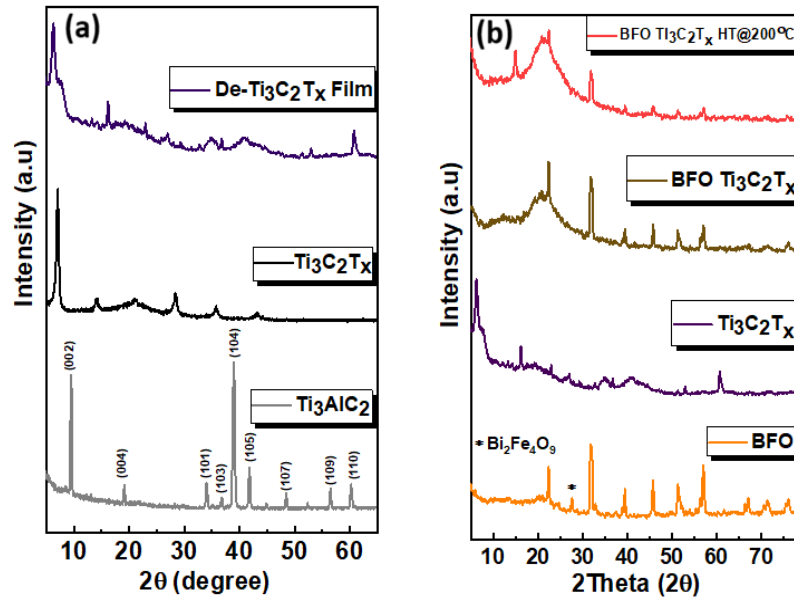
Figure 17 (a)XRD pattern of MAX, MXene and de-MXene (b) BFO@Ti$_3$C$_2$ Non-heated (NH) and heat- treated (HT) XRD comparision with Ti$_3$C$_2$T$_X$ and BFO.

0.154 nm) source was utilized in the 5 to 80° range.The XRD patterns Fig. 18(a) for Ti$_3$AlC$_2$ MAX, Ti$_3$C$_2$T$_X$ MXene, and de- Ti$_3$C$_2$T$_X$ reveal interesting structural changes. Upon reacting with HF for 24 hours, the most prominent peak at 2θ=38.95°, corresponding to the (104) characteristic peak of Ti$_3$AlC$_2$, significantly diminishes, indicating the removal of Al from Ti$_3$AlC$_{2[73]}$. Furthermore, the (002) peak, representing the basal planes of the two-dimensional titanium carbide layers, undergoes a noticeable shift from 2θ = 9.45° in the MAX phase to 7.1° in the MXene phase. This shift suggests structural expansion, likely due to the substitution of Al with oxygen-containing and/or fluoride functional groups[73]. Following delamination, there is a further shift, with the (002) peak reaching 6.3°. This shift is associated with a significant increase in the c-lattice

parameter, expanding from 18.6Å in the MAX phase to 28.6Å in the de-MXene phase. Additionally, the d-spacing expands from 9.2Å to 14.3Å in this transition.

The X-ray diffraction pattern of pure BFO nanoparticles is given in orange and $BFO@Ti_3C_2T_X$ structure is given in brown while HT- $BFO@Ti_3C_2T_X$ is shown in red color Fig.18(b). The XRD analysis reveals important insights into the structural changes caused by the incorporation of BFO nanoparticles into $Ti_3C_2T_x$ MXene, as well as the effects of high-temperature treatment (HT) on the composite material. Initially, the XRD pattern of pure BFO nanoparticles confirms their crystalline nature, which adopts a distorted rhombohedral structure with the R3c space group. This structure matches the known literature data (JCPDS 01-073-0548). The X-ray diffraction (XRD) peaks corresponding to the impurity phase at $2\theta=27.6^o$ in the BFO structure exhibit a strong resemblance to those found in the $Bi_2Fe_4O_9$ phase[67]. When BFO is added to $Ti_3C_2T_x$ MXene, the diffraction peaks of the MXene sheets become suppressed and less intense. This phenomenon is attributed to the distortion introduced by the BFO nanoparticles within the layered structure of $Ti_3C_2T_x$ MXene. Remarkably, the structure of BFO nanoparticles remains unaffected, as evidenced by the well-separated doublet peaks even after the formation of the $BFO@Ti_3C_2T_x$[67]. In the case of HT-BFO $Ti_3C_2T_x$, the XRD pattern shows slight oxidation reflections, which can be attributed to the presence of a low fraction and smaller-sized TiO_2 crystallites[63]. It's worth noting that room-temperature oxidation of MXene is a well-established phenomenon, and TiO_2 monoclinic phase peak at $2\theta = 15.05°$ (JCPDS 00-046-1237) is also observed. Further analysis indicates that heating BFO $Ti_3C_2T_x$ at 200°C for 2 hours leads to the suppression of the intensity of all composite peaks. This reduction in intensity can be attributed to the oxidation of $Ti_3C_2T_x$ MXene, which results in the consumption of Ti atoms and the formation of amorphous carbon[41]. Notably, the highly active Ti atoms in $Ti_3C_2T_x$ MXene play a crucial role in the formation of crystalline TiO_2. It is important to highlight that the oxidation of the $BFO@Ti_3C_2T_x$ composite is not complete, resulting in the presence of unreacted MXene in the core and oxide particles on the surface[41].

4.2: RAMAN spectroscopy:

Fig.19 shows Raman spectra of BFO, BFO@$Ti_3C_2T_X$(NH) and BFO@$Ti_3C_2T_X$(HT) in orange,
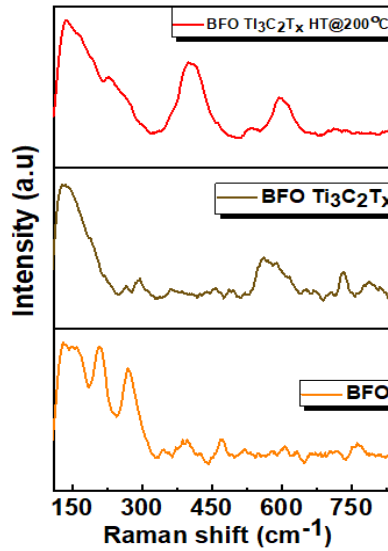

Figure 18 Raman spectra of pristine BFO, BFO@$Ti_3C_2T_X$(NH) and BFO@$Ti_3C_2T_X$ (HT)

brown and red color respectively at room temperature measured in the frequency range 100–800 cm^{-1}. BFO exhibits rhombohedral symmetry with the space group R3c. The group theory predicts that the 18 optical phonon modes in $BiFeO_3$ films with rhombohedral R3c structure exist 4A1+5A2+9E. While the A2 modes are Raman- and IR inactive, the A1 and E modes are Raman- and IR active[74]. Low frequency vibrational modes (less than 400 cm^{-1}) in the perovskite unit exhibit the preferred state of the Bi atoms, according to the Raman spectra investigation, but high frequency vibrational modes (more than 400 cm^{-1}) are associated with the stretching vibration of the Fe atoms in the FeO6 octahedral structure. The vibrational modes at frequency 130.6 and 207.6 cm^{-1}, designated A$_1$-1, and A$_3$-3, respectively, relate to covalent bonds between the Bi-O and distortions brought on by the Bi atoms at the tetrahedral site. Separation of the A$_1$-1 mode for BFO can result from secondary phase. The stretching vibrations of the Fe atoms in the FeO$_6$ octahedron are represented by the h A$_4$-4 vibrational mode at 467.6cm^{-1}. The ferroelectric distortion is associated with the E vibrational mode about 270 cm^{-1}, while the internal stretching of FeO$_6$ octahedra causes the other E vibrational modes to arise around 606.45cm^{-1}[75].

$Ti_3C_2T_x$ unit cell, that belongs to the point group D3d, vibrations are represented (in Mulliken symbols) as 2A$_{1g}$ + 4E$_g$+ 4E$_u$ + 2A$_{2u}$. E$_g$ and A$_{1g}$ are Raman active vibrations while E$_u$ and A$_{2u}$ are

IR active. E_g is an in-plane Ti and C atom vibration, and A_{1g}, an out-of-plane Ti and C atom vibration. The range 230-470 cm^{-1}, which is depicted as 295.54 cm^{-1} in our raman spectra, represents the in-plane (Eg) vibrations of surface groups attached to titanium atoms. Most of the carbon vibrations (both E_g and A_{1g}) are allocated to the region between 580 and 730 cm^{-1} shown by peaks at 561 and 589.9cm^{-1} in our raman spectra. Lattice vibrations may be influenced by different surface terminations, intercalated species, and adsorbed species. Peak shifting and broadening are caused by surface group dispersion and unit cell deformation[76]. So as result of BFO intercalation the A_{1g} peak in $Ti_3C_2T_X$ which appears around 720cm^{-1} is shifted to 732cm^{-1}. This greater interlayer spacing brought on can be explained as BFO intercalation into de- $Ti_3C_2T_X$ layers. Sharp peak at 133.23cm^{-1} is attributed as A_1-1 BFO peak. If we compare BFO@$Ti_3C_2T_X$ (HT) to BFO@$Ti_3C_2T_X$ (NH) sample, we can see shift in peak from 133.23 cm^{-1} to 138.27cm^{-1} due to oxidation. Peak at 401.8 cm^{-1} also shows vibrations of oxidized titanium atoms. 599.25cm^{-1} shows carbon vibrations.

4.3 SEM:

Fig. 20 (a) and (b) The SEM images of the BFO@$Ti_3C_2T_x$ MXene film reveal the successful formation of a
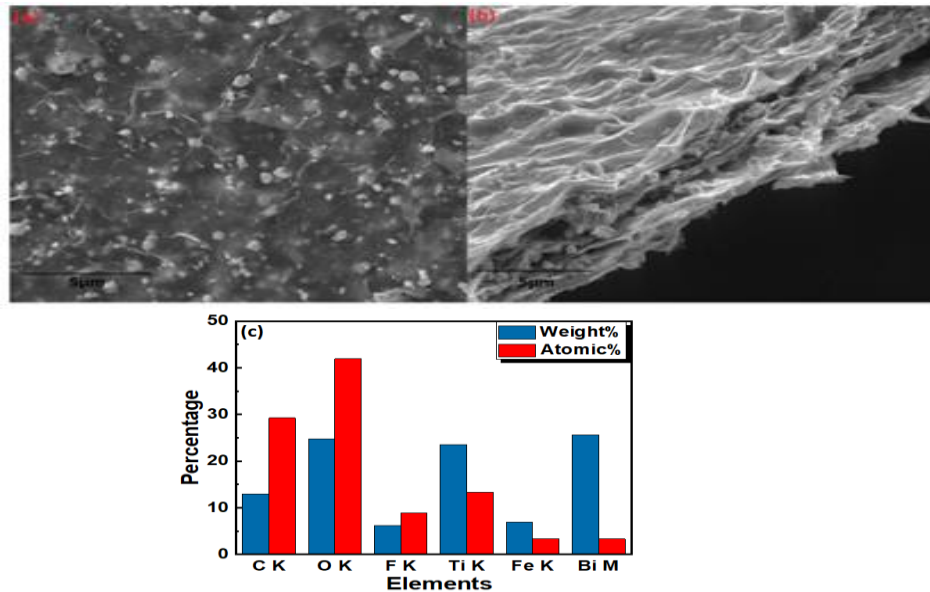

Figure 19 (a) shows surface morphology of BFO@$Ti_3C_2T_X$ (b) cross sectional view of BFO@$Ti_3C_2T_X$ (c) is telling about atomic and weight % of different elements in BFO@$Ti_3C_2T_X$

35

distinct layered structure, with evident sheet stacking and the presence of intercalated BFO nanoparticles (NPs) both between the sheets and on the film's surface.

4.4 Ferroelectric (FE) and multiferroic testing:

The ferroelectric and multiferroic properties were examined at room-temperature in two types of BFO@$Ti_3C_2T_X$ films: non-heated (NH) free-standing films and heat-treated (HT) films exposed to a temperature of 200°C in an oven having thickness of 34.5 μm and dimensions of 0.3 cm x 0.3 cm at room-temperature using **Precision Multiferroic II (Precision Material Analyzer); Radiant Technologies Inc.**

4.4.1 Polarization versus electric field hysteresis loop (PE loops):
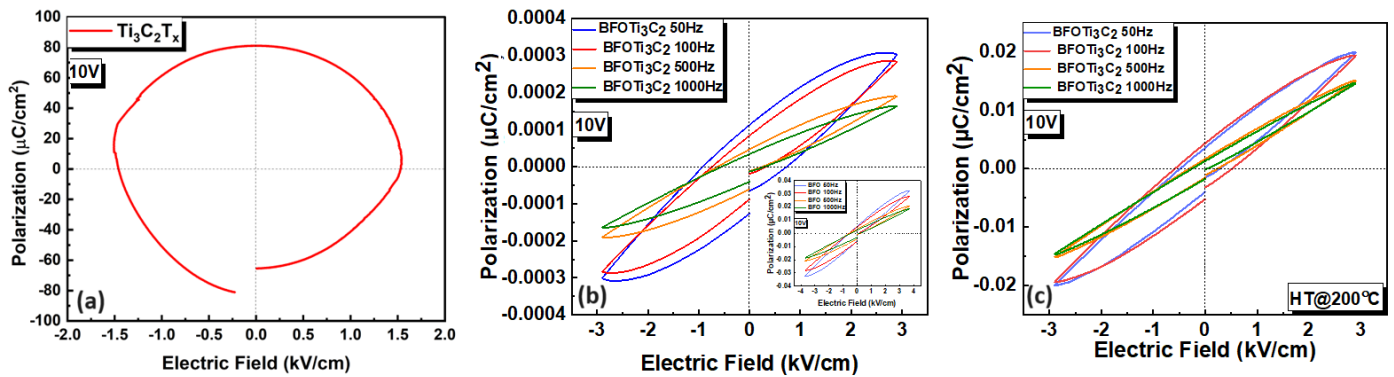
Figure 20 (a)non-FE pristine $Ti_3C_2T_X$ PE loop (b) PE loops of BFO@$Ti_3C_2T_X$ (NH) while (c) shows BFO@$Ti_3C_2T_X$ (HT) PE loops.

Fig. 21(a) Pristine $Ti_3C_2T_X$ is non ferroelectric at room temperature. Fig. 21(b) shows FE behavior of BFO@$Ti_3C_2T_X$. BFO is well known room temperature FE. The dominant factor behind FE behavior in $BiFeO_3$ is the involvement of Bi $6s^2$ lone pairs. These lone pairs actively participate in the hybridization of Bi-O orbitals, consequently leading to the development of ferroelectric characteristics within the material[13]. On intercalation in Pristine $Ti_3C_2T_X$, BFO has caused structural deformation in 2D layered MXene structure that can function as initiation points for the

movement of electric domain walls, leading to polarization values during the switching process. PE loops of BFO@$Ti_3C_2T_X$(NH) sample at different frequencies from 50Hz to 1000Hz at 10V have been reported. Coercive fields exhibit strong frequency dependence because altering the electric field within a material involves shifting of electric domains through a material. The resistance experienced by domains varies significantly depending on the speed at which the change is attempted[77]. At higher frequencies, some of the electric domains become unable to respond to the applied electric field, leading to a noticeable decline in the material's both saturation polarization (P_S) and remanent polarization (P_r)[78] that can be seen in fig 21(b) as we go from 50Hz to 1000Hz both P_s and P_r has been decreased. The observed hysteresis loops show a notable loop opening, and this phenomenon can be explained by considering the sample's ability to retain charge and its finite resistivity, which leads to charge leakage through conduction[79].

Fig. 21c displays the ferroelectric hysteresis loops (PE loops) of BFO@$Ti_3C_2T_X$ (HT) at 10V, covering a frequency range from 50Hz to 1000Hz. Notably, there is a substantial alteration in the values of P_s and P_r following the heat treatment process. Specifically, after heat treatment at 10V and 50Hz, P_s has transitioned from 0.0003$\mu C/cm^2$ to 0.02$\mu C/cm^2$, while P_r has shifted from 0.0001$\mu C/cm^2$ to 0.003$\mu C/cm^2$. The intensified polarization effect could be a consequence of an insufficiently developed TiO_2 phase on surface of BFO@$Ti_3C_2T_X$ (HT) [63, 64].

We suppose that when BFO@$Ti_3C_2T_X$ (HT) undergoes oxidation through heating, it initiates the homogeneous nucleation of TiO_2 nanoparticles. This nucleation process occurs on both the upper and lower Ti layers, which are directly exposed to oxygen. Consequently, the oxidation process yields TiO_2 nanoparticles that find support on carbon sheets. We assume that the entire top and bottom Ti layers initially undergo a transformation. This transformation is not localized to specific sites but occurs uniformly throughout these layers due to non-site-specific nucleation. Subsequently, a diffusion process follows, with Ti atoms from the middle layer migrating towards the oxygen source.

In fig. 22(a) BFO@$Ti_3C_2T_X$ (NH) and fig.22(b) BFO@$Ti_3C_2T_X$ (HT) PE loops under applied static magnetic field of 900Oe and 3000Oe are compared with PE loops at 0Oe. The difference observed in the P-E loops when comparing situations with and without the presence of magnetic fields serves as a clear indication of the magnetic field's influence on electric polarization[64]. When a magnetoelectric material is exposed to a magnetic field, it undergoes strain, resulting in the
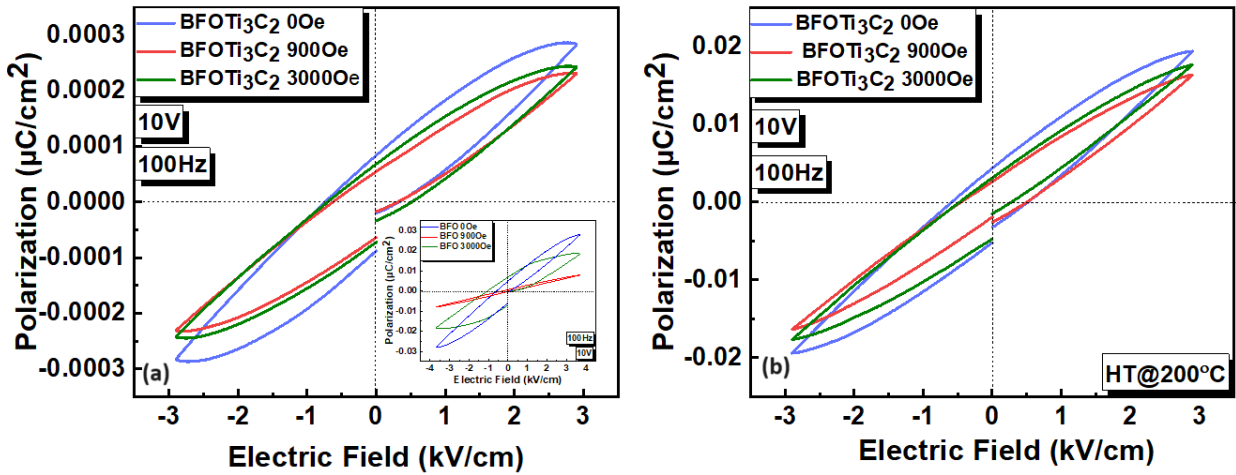
Figure 21(a) BFO@Ti$_3$C$_2$T$_X$ (NH) PE loops at different values of static magnetic field (b) BFO@Ti$_3$C$_2$T$_X$ (HT) PE loops at different values of static magnetic field.

This stress, in turn, leads to the production of an electric field. This electric field has the potential to align the domains within the ferroelectric material. The connection between magnetic and ferroelectric domains leads alteration of the ferroelectric behavior[80]. This discovery opens exciting prospects for manipulating ferroelectric domains through magnetic fields, providing strong evidence for the existence of strong magnetoelectric (ME) coupling in BFO@Ti$_3$C$_2$T$_X$ films at room temperature.

4.4.2 Magnetoelectric (ME) coupling

Fig. 23 (a) and (b) are showing BFO@Ti$_3$C$_2$T$_X$ (NH) and fig. 23 (c) and (d) are showing BFO@Ti$_3$C$_2$T$_X$ (HT) ME coupling coefficient (dP/dH) versus applied magnetic field at 10Hz. The MH loop demonstrates the indication of magnetic behavior in BFO@Ti3C2TX film, which is

Figure 22(a) and (b) presents ME coupling of BFO@Ti$_3$C$_2$T$_X$(NH) at 900Oe and 3000Oe respectively while (c) and(d) presents ME coupling of

attributed to the ferromagnetic properties exhibited by BFO (Bismuth Ferrite Oxide). The origin of magnetoelectric (ME) coupling in multiferroic Bismuth Ferrite (BFO) can be elucidated by

considering the "spin current" model. This model establishes a connection between ferroelectricity and the spin-orbit interaction, known as the Dzyaloshinskii-Moriy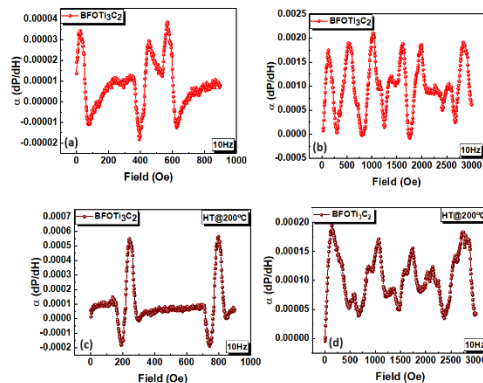a interaction. According to this model, the presence of bond bending, specifically in the Fe-O-Fe bonds within BFO, can induce ferroelectricity and enhance the voltage coefficient for ME effects[81]. In the case of the ME effect, when a magnetic field is introduced to a composite material, the magnetic phase undergoes magneto strictive changes in its shape. This deformation or strain is subsequently transmitted to the adjacent piezoelectric phase, ultimately leading to the generation of electric polarization within the material[82]. The magnetoelectric effect, as represented by the change in polarization (dP/dH), initially intensifies with an increased magnetic field. However, a continued rise in the magnetic field leads to a reduction in the dP/dH value. To put it differently, the application of a magnetic field induces the alignment of magnetic domains in its direction, resulting in magnetostriction-induced stress on the electric domains for alignment. Yet, when the magnetic domains are completely aligned, no additional strain is transferred to the electric domains, resulting in a decline in dP/dH values[83].

4.4.3 Leakage current:

Fig.24(a) shows BFO@Ti$_3$C$_2$T$_X$ (NH) and Fig.24(b) shows BFO@Ti$_3$C$_2$T$_X$ (HT) leakage current loops. As
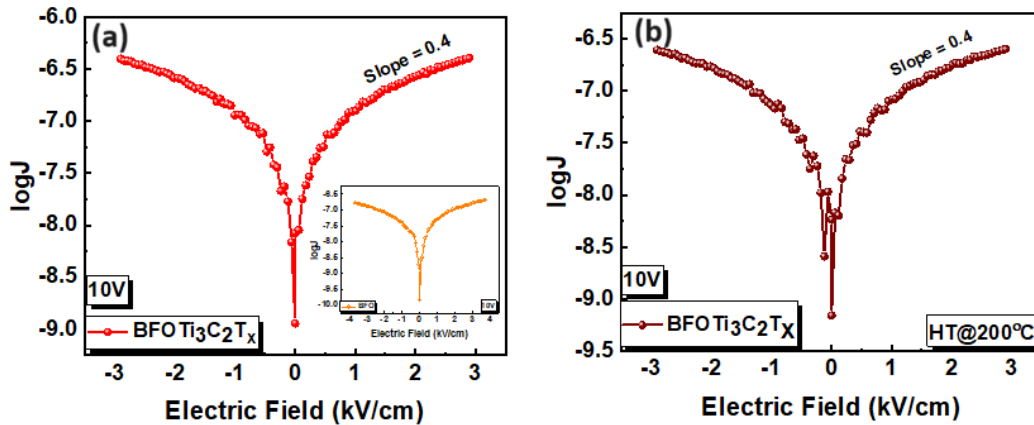
Figure 23 (a) BFO@Ti$_3$C$_2$T$_X$ (NH) leakage currect at 10V (b) BFO@Ti$_3$C$_2$T$_X$ (HT) leakage current at 10V

we go from BFO@Ti$_3$C$_2$T$_X$ (NH) to BFO@Ti$_3$C$_2$T$_X$ (HT) leakage current through film decreases. This variation can be linked to alterations in the conduction mechanism of leakage current due to structural transformations. Leakage current might result from trapped carriers moving from the band gap to the conduction band due to an applied field that changes defect potentials. This current is influenced by the distribution of defect levels within the film, which varies with temperature and applied field strength[84].

There is an almost linear increase in leakage current Fig.24 (a) and (b) with a slope of approximately 0.4, it illustrates the relationship between logsJ $\propto$ E.

4.4.4 Dielectric constant:

Dielectric constant versus voltage loops in fig. 25 (a) and (b) had displayed the typical butterfly-shaped pattern commonly associated with ferroelectrics[85, 86]. Due to small poling, the dielectric constant is initially low; nevertheless, it grows at higher voltages and reaches its maximum at about coercive voltages. near the polarization's saturation values[63, 87]. The movement of domain walls
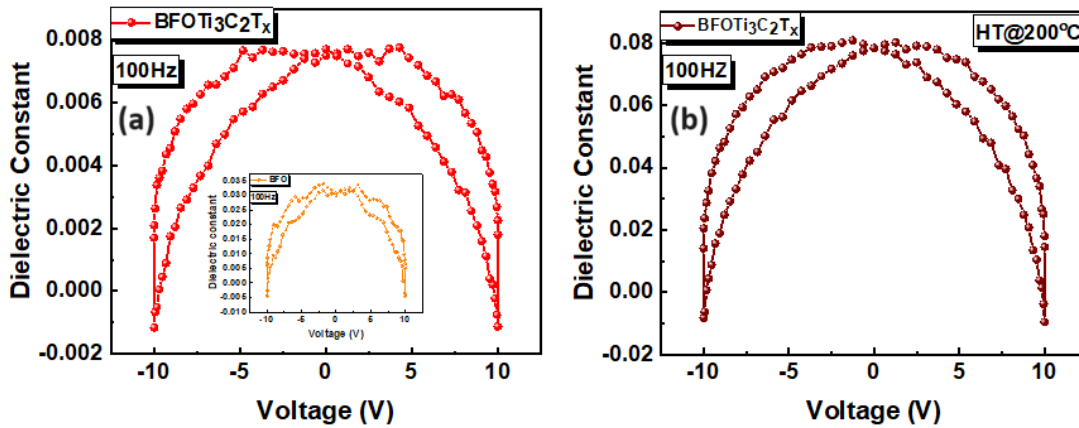
Figure 24 (a) Dielectric constant versus voltage loop for BFO@Ti$_3$C$_2$T$_X$ (NH) at 100Hz (b) Dielectric constant versus voltage loop for BFO@Ti$_3$C$_2$T$_X$ (HT) at100Hz

redistributes electric fields at domain interfaces. Few negative values of the dielectric constant are caused by the redistribution of electric fields at domain interfaces caused by the movement of domain walls. This redistribution reduces the material's overall energy and negatively impacts its ability to store electric charge per unit voltage, a key feature of negative capacitance behavior[88].

Chapter 5: Results and discussion $Z_{12}@Ti_3C_2T_X$ and $Z_{13}@Ti_3C_2T_X$

5.1: 5.1 X-Ray Diffraction (XRD):

X-ray diffraction (XRD) analysis was conducted on samples, including BFO, Z_{12}, and Z_{13} Figure
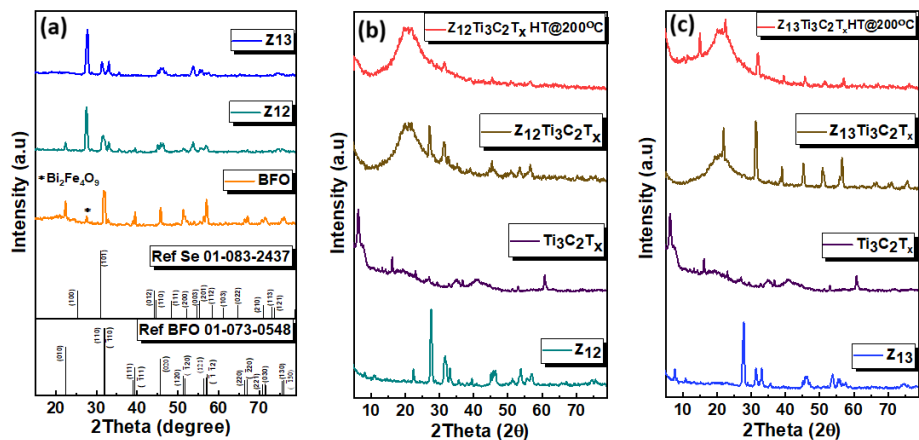
Figure 25 (a)XRD pattern of BFO, Z12 and Z13 (b) comparison of $Z_{12}@Ti_3C_2$ (NH) and $Z_{12}@Ti_3C_2$ XRD (HT) (c) comparison of $Z_{13}@Ti_3C_2$ (NH) and $Z_{13}@Ti_3C_2$ (HT) XRD

19(a) presents their XRD results. The XRD pattern of BFO closely matches the reference pattern of Bismuth Iron Oxide #01-073-0548, indicating a rhombohedral structure corresponding to the R3C space group, with a $Bi_2Fe_4O_9$ phase impurity. In Z_{12} and Z_{13}, due to the difference in ionic radii between Se^{+4} (0.64 Å) [89] and Bi^{+3} (1.03 Å) [90], Se^{+4} is likely substituting Fe^{+3} ions (0.78 Å) [91]. Because Se^{+4} has a smaller ionic radius than Fe^{+3}, a clear peak shift toward higher angles was observed in the $(1\bar{1}0)$ plane, resulting in a decreased interplanar distance. As a result of Se^{+4} doping, the singlet peak at $2\theta = 45.6$ transforms into a triplet, and the intensity of some peaks is reduced.

Figure 19(b) compares the XRD patterns of $Z_{12}@Ti_3C_2$ (NH) and $Z_{12}@Ti_3C_2$ (HT). $Z_{12}@Ti_3C_2$ (NH) is shown in brown. When Z_{12} is added to $Ti_3C_2T_x$ MXene, the diffraction peaks of the MXene sheets become less intense and suppressed. This phenomenon is attributed to the distortion introduced by Z_{12} nanoparticles within the layered structure of $Ti_3C_2T_x$ MXene. Peaks at $2\theta = 27.1$ and 53.3 indicate the coexistence of a cubic phase (JCPDS 01-077-0568) along with a rhombohedral phase. In the $Z_{12}@Ti_3C_2$ (HT) structure shown in red, all the peaks are further suppressed. This reduction in intensity is likely due to the oxidation of $Ti_3C_2T_x$ MXene, leading to the consumption of Ti atoms and the formation of amorphous carbon. In the case of HT, oxidation reflections are not visible, likely because of the presence of a low fraction and smaller-sized TiO2 crystallites[63].

Fig. 19(c) illustrates the characterization of Z_{13}@Ti_3C_2 (HT) and Z_{13}@Ti_3C_2 (NH) composites. The addition of Z_{13} to $Ti_3C_2T_X$ introduces a secondary cubic phase (indexed as JCPDS 01-077-0568), alongside the rhombohedral phase present in Z_{13}. This combination of materials distorts the MXene structure, as evidenced by the diminished $Ti_3C_2T_X$ peaks. In the Z_{13}@Ti_3C_2 HT-treated sample, there is a distinct peak at $2\theta = 15.0°$ corresponding to the monoclinic phase of TiO_2 (indexed as JCPDS 00-046-1237). This reduction in peak intensity is attributed to the oxidation of $Ti_3C_2T_x$ MXene, resulting in the consumption of Ti atoms and the creation of amorphous carbon[41]. This oxidation is further demonstrated by the heightened graphitic hump seen in Figure 19(b-c) HT XRD pattern at $2\theta \approx 21°$ [92]. Notably, in the HT sample, the oxidation reflections are less pronounced due to the lower proportion and smaller-sized TiO_2 crystallites present in this material[63].

5.2 Raman spectroscopy:
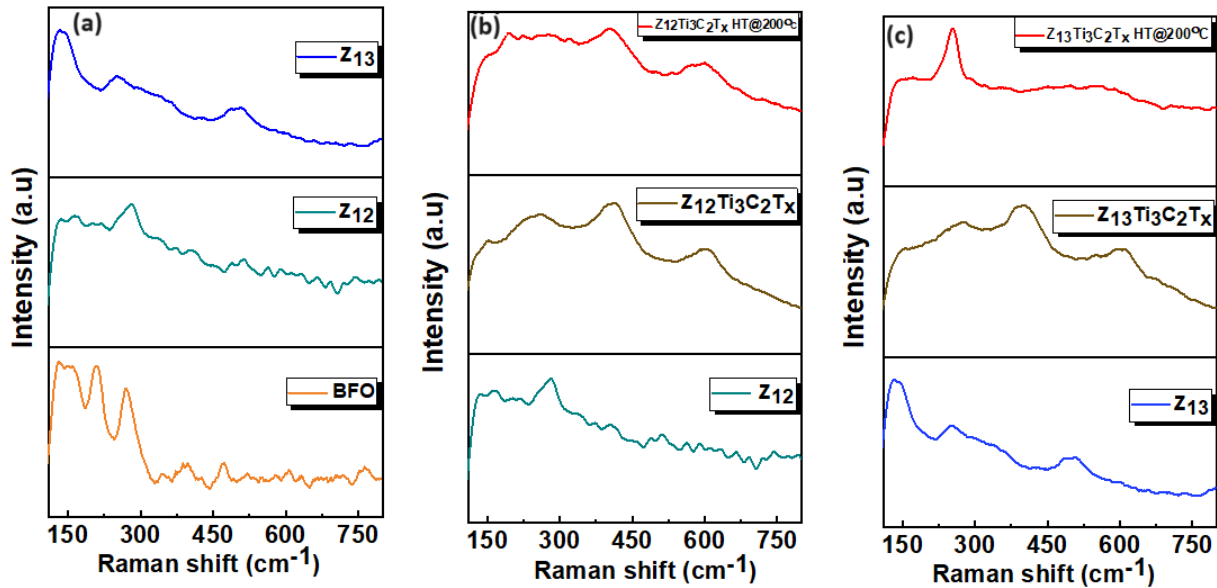
Figure 26 (a) shows comparison of BFO with Z_{12} and Z_{13} Raman spectra (b) shows raman spectra of Z_{12}, Z_{12}@$Ti_3C_2T_X$(NT) and Z_{12}@$Ti_3C_2T_X$(HT) (b) raman spectra of Z_{13},Z_{13}@$Ti_3C_2T_X$(NT) and Z_{13}@$Ti_3C_2T_X$(HT)

Fig.22(a) shows comparison of BFO with Z_{12} and Z_{13}. The group theory analysis predicts the presence of 13 optical active Raman modes (with a symmetry group R3c) in rhombohedral BFO. These modes are categorized into $4A_1+ 9E$ modes [93]. The Raman spectra measurements reveal that the occupation states of the bismuth atoms within the perovskite unit are linked to the low-

frequency modes (below 400 cm^{-1}), whereas the vibrations of the iron atoms within FeO6 octahedra are associated with the high-frequency modes. Specifically, the covalent bonding between bismuth and oxygen atoms is primarily governed by the first three A1 modes (A$_1$-1, A$_1$-2, and A$_1$-3), in addition to one E mode (around 260 cm^{-1}), which is responsible for inducing the ferroelectric distortion [94]. As the Selenium (Se) doping in BFO increases from 0 to 0.75, there is a continuous upward shift in the Raman modes towards higher frequency values indicating that Se atoms are likely replacing iron (Fe) atoms in the BiFeO$_3$ lattice. It is noteworthy that the intensity of the A1-1 Raman mode remains stronger than that of A$_1$-2. This observation suggests that the Bi-O bonds are stable [95]. The one E mode associated with ferroelectric distortions around 260cm-1 is also intense and slightly shifted in Z$_{12}$ and Z$_{13}$ showing ferroelectric behavior of lattice. The shifting of E modes can be attributed to lattice distortions, alterations in bond lengths, and changes in bond angles within the intercalated BFO. These modifications are linked to the vibrations of Fe atoms within the FeO6 octahedra, which are primarily associated with high-frequency modes. Fig 22 (b) and (c) present raman spectra of Z$_{12}$@Ti$_3$C$_2$T$_X$ (NH) and Z$_{12}$@Ti$_3$C$_2$T$_X$ (HT) and Z$_{13}$@Ti$_3$C$_2$T$_X$ (NH) and Z1$_3$@Ti$_3$C$_2$T$_X$ (HT). In the Ti$_3$C$_2$T$_x$ unit cell (D3d point group), vibrations include 2A$_1$g + 4Eg + 4Eu + 2A$_2$u. Eg and A$_1$g are raman-active vibrations. Eg is an in-plane Ti and C atom vibration, and A1g, an out-of-plane Ti and C atom vibration [7]6]. The spectral range between 230 and 470 cm-1 is indicative of in-plane (Eg) vibrations associated with titanium atoms. This observation is confirmed by the notable peaks found at 248 cm-1 and 406 cm-1 in the Raman spectra of Z$_{12}$@Ti$_3$C$_2$T$_X$ (NH), as well as at 273 cm^{-1} and 400.32 cm^{-1} in the case of Z$_{13}$@Ti$_3$C$_2$T$_X$ (NH). The 230 to 470 cm-1 range represents in-plane (Eg) vibrations attached to titanium atoms which is evident from the presence of prominent peaks at 248 cm-1 and 406cm-1 in Z$_{12}$@Ti$_3$C$_2$T$_X$ (NH) while in Z$_{13}$@Ti$_3$C$_2$T$_X$ (NH) at 273 and 400.32cm^{-1} in our raman spectra. In the case of carbon vibrations, both Eg and A1g modes are predominantly observed within the range of 580-730 cm^{-1}, with a specific peak observed at 590.9 cm^{-1} in Z$_{12}$@Ti$_3$C$_2$T$_X$ (NH) and 607.23 cm^{-1} in Z$_{13}$@Ti$_3$C$_2$T$_X$. Surface terminations, intercalation, and adsorption can affect lattice vibrations, causing peak shifts and broadening due to dispersion and unit cell deformation [76] which is shown by distorted and suppressed peak around 150 cm-1 in both Z$_{12}$@Ti$_3$C$_2$T$_X$ (NH) and Z$_{13}$@Ti$_3$C$_2$T$_X$. In Z$_{12}$@Ti$_3$C$_2$T$_X$ (HT) all the peaks are distorted and suppressed below 330cm^{-1} as result of oxidation only peaks at 400 cm^{-1} and 592.8 cm^{-1} are obvious showing the in-plane (Eg) vibrations attached to titanium atoms and carbon vibration. While in

$Z_{13}@Ti_3C_2T_X$ (HT) all peaks except sharp peak at 252.73 cm^{-1} almost disappeared as result of heating sample at 200°C showing the formation of TiO_2 phase as result of oxidation [96].

5.3 SEM:
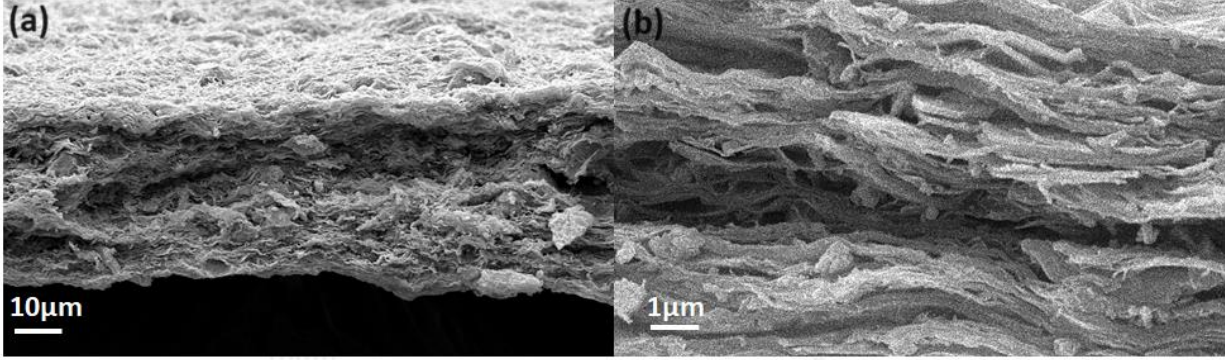
Figure 27 (a) and (b) shows $Z_{12}@Ti_2C_2T_X$ free standing film cross-sectional morphology at scale of 10 μm and 1 μm respectively.

Fig 23(a) and (b) The SEM images of the $Z_{12}@Ti_3C_2T_x$ MXene film reveal the successful formation of a distinct layered structure, with evident sheet stacking and the presence of intercalated BFO nanoparticles (NPs) between the sheets.

5.4 Ferroelectric and multiferroic testing:

The ferroelectric and multiferroic properties were examined at room-temperature in $Z_{12}@Ti_3C_2T_X$
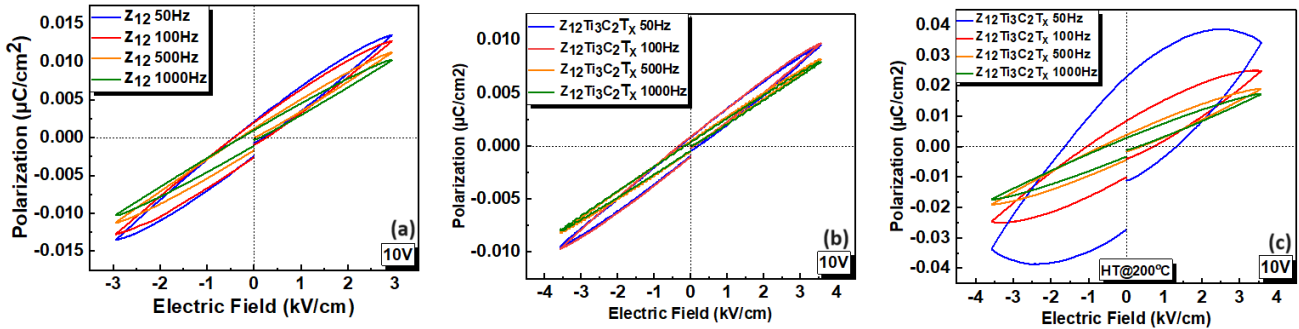
Figure 28 Figure 29 (a), (b) and (c) shows PE loops of Z_{12}, $Z_{12}@Ti_3C_2T_X$ (NH) and $Z_{12}@Ti_3C_2T_X$(HT) respectively at 10V.

and $Z_{13}@Ti_3C_2T_X$ films: non-heated (NH) free-standing films and heat-treated (HT) films exposed to a temperature of 200°C in an oven having dimensions of 0.4 cm x 0.4 cm at room-temperature using **Precision Multiferroic II (Precision Material Analyzer); Radiant Technologies Inc.**:

5.4.1: Polarization versus electric field hysteresis loop (PE loops):
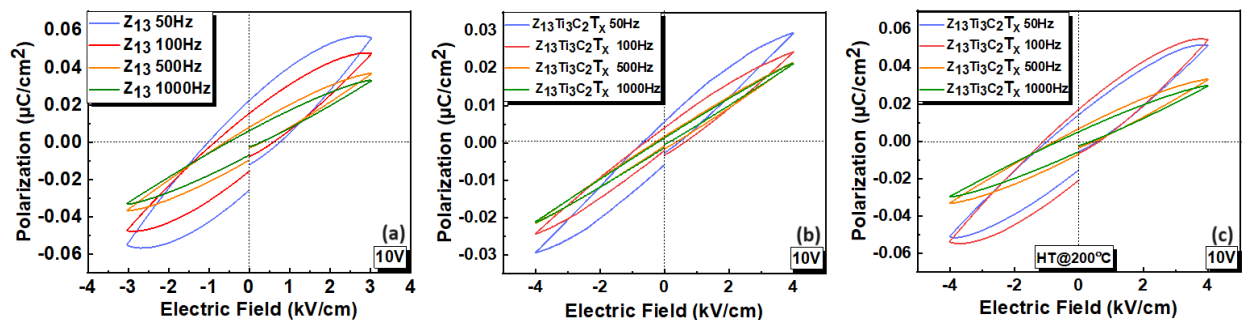
Figure 29 (a), (b) and (c) shows PE loops of Z_{13}, Z_{13}@$Ti_3C_2T_X$ (NH) and Z_{13}@$Ti_3C_2T_X$ (HT) respectively at 10V.

The trend becomes apparent when observing figures 29(a) and 30(a). As the selenium ratio in BFO P_s is gradually increased, there is a noticeable elevation in the polarization from 0.0125μC/cm² in Z_{12} to 0.05μC/cm² in Z_{13}. The behavior of the polarization-electric field graph confirms the ferroelectric characteristics of the samples, which result from domain switching and are further intensified with higher concentrations of Se.

The introduction of Z_{12} and Z_{13} to MXene figures 29(b) and 30(b) has led to a reduction in the polarization value when compared to the pristine Z_{12} and Z_{13}. This decrease can be attributed to the intercalation of Z_{12} and Z_{13} into the MXene structure, which has introduced a secondary cubic phase into the BFO structure.

After undergoing heat treatment, the polarization values have once again exhibited an increase when compared to the non-heat-treated samples, as illustrated in figures 29(c) and 30(c). When subjected to heat, oxidation takes place, triggering the uniform nucleation of TiO_2 nanoparticles. This nucleation phenomenon occurs simultaneously on both the upper and lower layers of titanium, which are directly exposed to oxygen. Importantly, this transformation doesn't localize to specific sites but instead spreads uniformly across these layers due to non-site-specific nucleation. Subsequently, a diffusion process ensues, with titanium atoms from the middle layer migrating towards the oxygen source.
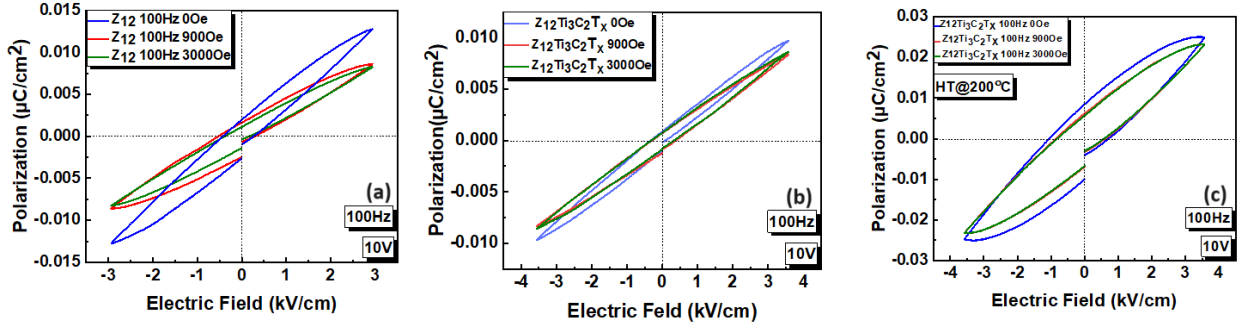
Figure 30(a), (b) and (c) shows effect of static magnetic field on Z_{12}, $Z_{12}@Ti_3C_2T_X$ (NH), $Z_{12}@Ti_3C_2T_X$ (HT) PE loops respectively.
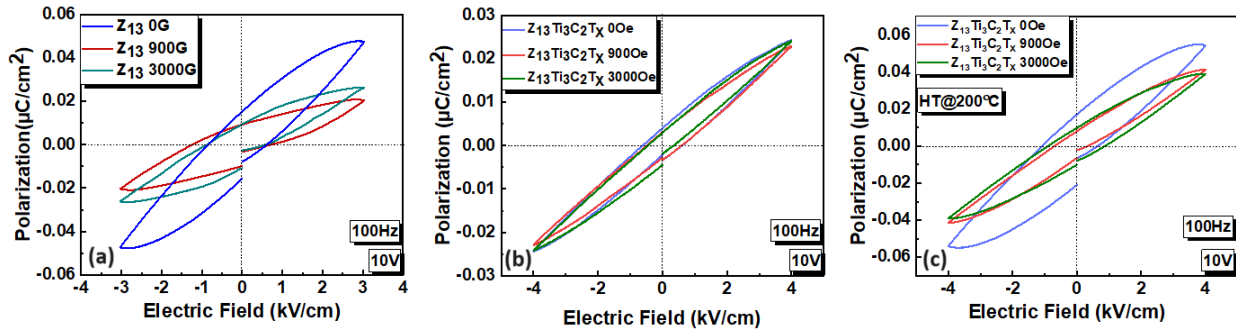
Figure 31 (a), (b) and (c) shows effect of static magnetic field on Z_{13}, $Z_{13}@Ti_3C_2T_x$ (NH), $Z_{13}@Ti_3C_2T_x$ (HT) PE loops respectively.

In Figure 31 and 32, we compare the PE loops of prepared sample under static magnetic fields of 900Oe and 3000Oe to those at 0Oe. This difference in the P-E loops clearly demonstrates the influence of magnetic fields on electric polarization[64]. When a magnetoelectric material is exposed to a magnetic field, it undergoes strain, leading to mechanical stress within the piezoelectric material (as all ferroelectrics are piezoelectric). This stress, in turn, generates an electric field capable of aligning domains within the ferroelectric material[80]. This connection between magnetic and ferroelectric domains alters ferroelectric behavior, highlighting strong magnetoelectric coupling in prepared films at room temperature and promising possibilities for controlling ferroelectric domains through magnetic fields.

5.4.2 Magnetoelectric (ME) coupling:
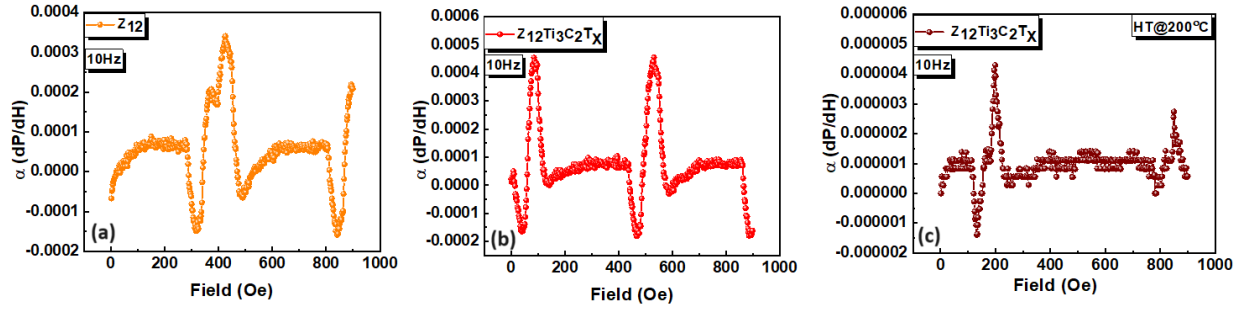
Figure 32 (a), (b) and (c) shows Z_{12}, $Z_{12}@Ti_3C_2T_X$ (NH) and $Z_{12}@Ti_3C_2T_x$ (HT) ME coupling coefficient(dP/dH) versus magnetic field graphs at 10Hz.
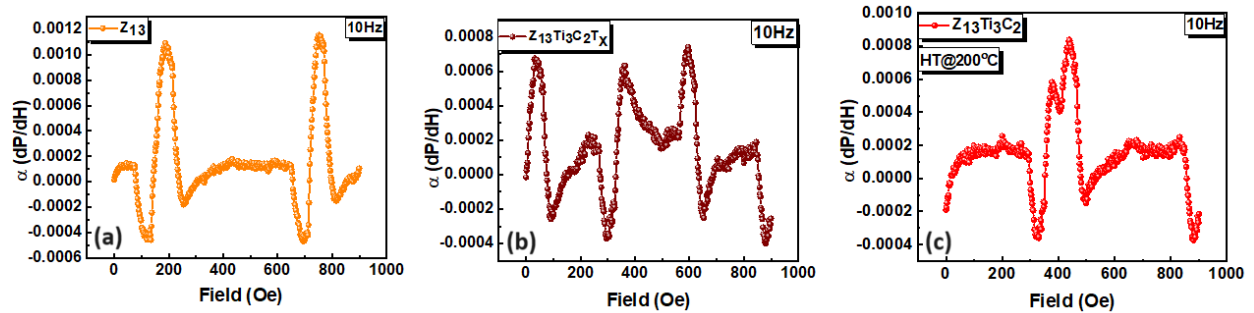
Figure 33 (a), (b) and (c) shows Z_{13}, $Z_{13}@Ti_3C_2T_X$ (NH) and $Z_{13}@Ti_3C_2T_x$ (HT) ME coupling coefficient(dP/dH) versus magnetic field graphs at 10Hz.

The relationship between Se doping and (dP/dH) is evident in figures 33(a) and 34(a), where an increase in Se doping corresponds to an increase in the dP/dH value. It's worth noting that a higher magnetization level within a specific sample is also associated with a greater potential for the magnetoelectric (ME) effect to be more pronounced in that sample. The magnetoelectric effect, indicated by the change in polarization (dP/dH), initially strengthens with a higher magnetic field. Nevertheless, as the magnetic field continues to increase, the dP/dH value starts to decrease. To put it another way, when a magnetic field is applied, it prompts the alignment of magnetic domains in its direction, causing stress on the electric domains due to magnetostriction-induced alignment. However, when the magnetic domains reach full alignment, there is no further strain transferred to the electric domains, leading to a reduction in dP/dH values [82].

5.4.3 Leakage current:
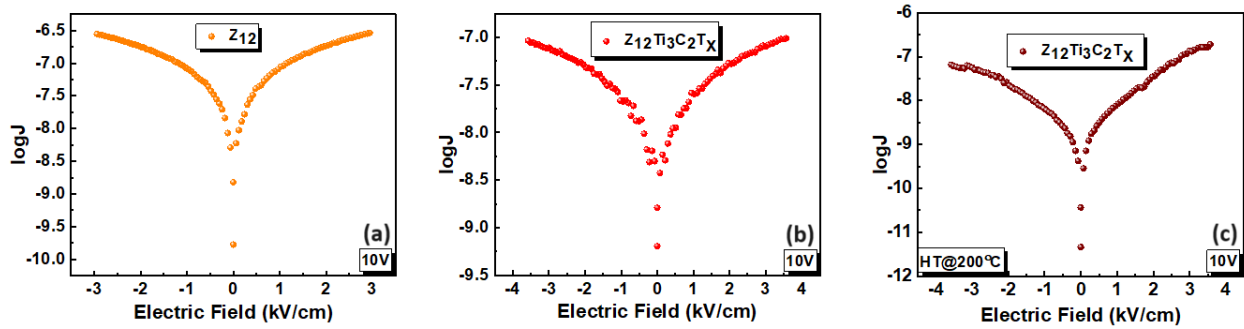
Figure 34 (a), (b) and (c) shows leakage current across Z_{12}, $Z_{12}@Ti_3C_2T_X(NH)$ and $Z_{12}@Ti_3C_2T_X$ (HT) free standing film
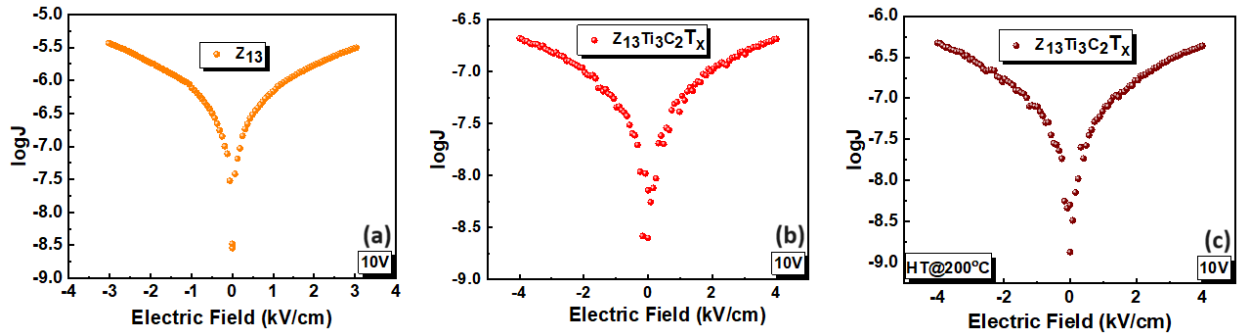
Figure 35 (a), (b) and (c) shows leakage current across Z_{13}, $Z_{13}@Ti_3C_2T_X$ (NH) and $Z_{13}@Ti_3C_2T_X$ (HT) free standing film.

As the level of Se doping in BFO increases, a notable phenomenon emerges - an increase in the leakage current. This phenomenon can be attributed to the heightened distortion within the crystal structure. This current's behavior is intricately linked to the distribution of defect energy levels within the film, and this distribution undergoes variations with changes in temperature and the strength of the applied electric field[84]. This relationship between the leakage current and these factors can be visually represented, showing an almost linear increase as depicted. This serves to illustrate the correlation between the logarithm of the current (logsJ) and the applied electric field (E) to be linear.

5.4.3 Dielectric constant:

The dielectric constant increases as we transition from Z_{12} to Z_{13} due to rising polarization saturation (P_S). In Figure 37 and 38, the characteristic butterfly-shaped pattern commonly seen in ferroelectrics is displayed [84, 85]. Initially, the dielectric constant is low due to minimal poling, but it increases at higher voltages, peaking near coercive voltages and polarization saturation [62, 86].
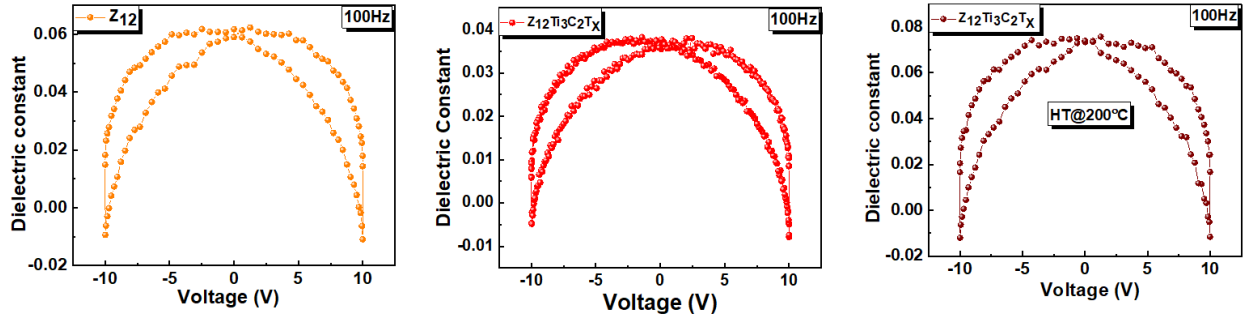
Figure 36 (a), (b) and (c) shows Z_{12}, $Z_{12}@Ti_3C_2T_X$ (NH) and $Z_{12}@Ti_3C_2T_x$ (HT) dielectric constant butterfly loops at 100Hz.
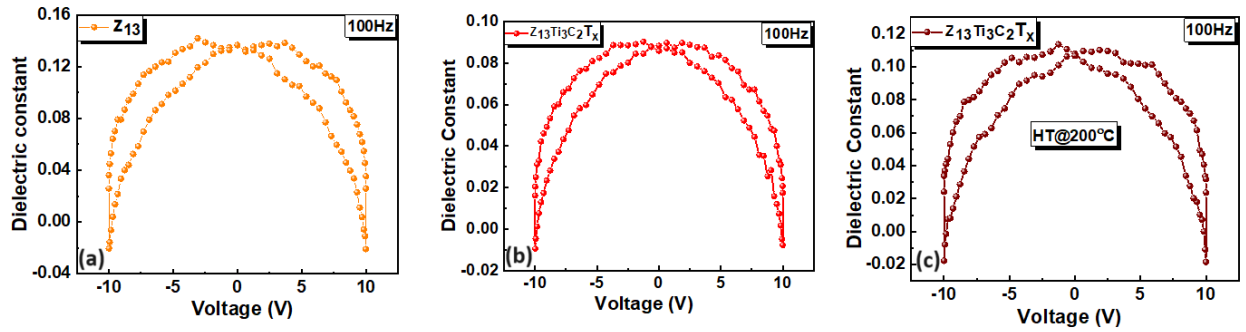
Figure 37 (a), (b) and (c) shows Z_{13}, $Z_{13}@Ti_3C_2T_X$ (NH) and $Z_{13}@Ti_3C_2T_x$ (HT) dielectric constant butterfly loops at 100Hz.

The movement of domain walls alters electric field distribution at domain interfaces. Some negative dielectric values restrict from this redistribution, which reduces the material's overall energy and hinders its ability to store electric charge per unit voltage[88].

Chapter 6: Conclusion

BFO@Ti$_3$C$_2$T$_x$, Z$_{12}$@Ti$_3$C$_2$T$_x$, and Z$_{13}$@Ti$_3$C$_2$T$_x$ non heated and heat-treated free-standing films were prepared adopting a very simple synthesis approach. XRD patterns as well as Raman spectra of these free-standing films showed suppression of Ti$_3$C$_2$T$_x$ peaks due to presence of large size BFO, Z$_{12}$ and Z$_{13}$ intercalated nanoparticles. As previously reported, Ti$_3$C$_2$T$_x$ is non-ferroelectric. However, when BFO, Z$_{12}$, and Z$_{13}$ are intercalated into free-standing films of Ti$_3$C$_2$T$_x$, the ferroelectric measurements reveal a distinct and easily distinguishable P-E hysteresis loop, indicating an enhanced polarization and magnetoelectric (ME) coupling. After undergoing heat treatment, the ferroelectric results become even more pronounced, which is attributed to the formation of the TiO2 phase within the MXene material. Hence, we were successful in inducing ferroelectric and multiferroic behavior at room temperature in 2D Ti$_3$C$_2$T$_X$. This investigation is a step forward for potential application of BFO@Ti$_3$C$_2$T$_x$, Z$_{12}$@Ti$_3$C$_2$T$_x$ and Z$_{13}$@Ti$_3$C$_2$T$_x$ free standing film in electronic and data storage devices.

Referrences

1.   Devonshire, A.J.A.i.p., *Theory of ferroelectrics.* 1954. **3**(10): p. 85-130.

2.   Park, M.H., et al., *Review and perspective on ferroelectric HfO2-based thin films for memory applications.* 2018. **8**(3): p. 795-808.

3.   Kittel, C., *Introduction to solid state physics*. 2005: John Wiley & sons, inc.

4.   Ulaby, F.T. and U. Ravaioli, *Fundamentals of applied electromagnetics*. Vol. 7. 2015: Pearson Upper Saddle River, NJ.

5.   Khikhlovskyi, S.V.V. and G.J.U.o.G. Blake, *The renaissance of multiferroics: bismuth ferrite (BiFeO3)– a candidate multiferroic material in nanoscience.* 2010. **1**(3).

6.   Hill, N.A.J.T.j.o.p.c.B., *Why are there so few magnetic ferroelectrics?* 2000, ACS Publications. p. 6694-6709.

7.   Weiss, P.J.J.p., *Hypothesis of the molecular field and ferromagnetic properties.* 1907. **4**(6): p. 661-690.

8.   Martin, L., et al., *Multiferroics and magnetoelectrics: thin films and nanostructures.* 2008. **20**(43): p. 434220.

9.   Schmid, H.J.F., *Multi-ferroic magnetoelectrics.* 1994. **162**(1): p. 317-338.

10.   Ascher, E., et al., *Some properties of ferromagnetoelectric nickel-iodine boracite, Ni3B7O13I.* 1966. **37**(3): p. 1404-1405.

11.   Hur, N., et al., *Electric polarization reversal and memory in a multiferroic material induced by magnetic fields.* 2004. **429**(6990): p. 392-395.

12.   Ramesh, R. and N.A.J.N.m. Spaldin, *Multiferroics: progress and prospects in thin films.* 2007. **6**(1): p. 21-29.

13.   Sivaraj, K., et al., *Sillenite phase stabilized ferromagnetic ordering in multiphasic magnetoelectric bismuth ferrite.* 2021. **299**: p. 122162.

14.   Khomskii, D.J.P., *Classifying multiferroics: Mechanisms and effects.* 2009. **2**: p. 20.

15.   Freeman, A.J. and H. Schmid, *Magnetoelectric interaction phenomena in crystals*. 1975: Gordon & Breach Publishing Group.

16.   Paras, et al., *A Review on Low-Dimensional Nanomaterials: Nanofabrication, Characterization and Applications.* 2022. **13**(1): p. 160.

17.   Sudha, P.N., et al., *Nanomaterials history, classification, unique properties, production and market*, in *Emerging applications of nanoparticles and architecture nanostructures*. 2018, Elsevier. p. 341-384.

18.   Tiwari, J.N., R.N. Tiwari, and K.S.J.P.i.M.S. Kim, *Zero-dimensional, one-dimensional, two-dimensional and three-dimensional nanostructured materials for advanced electrochemical energy devices.* 2012. **57**(4): p. 724-803.

19.   Kalantari, M.H. and X.J.N. Zhang, *Thermal Transport in 2D Materials.* 2022. **13**(1): p. 117.

20.   Novoselov, K.S., et al., *Electric field effect in atomically thin carbon films.* 2004. **306**(5696): p. 666-669.

21.   Persson, I., *Surface characterization of 2D transition metal carbides (MXenes)*. Vol. 1986. 2019: Linköping University Electronic Press.

22.   Barsoum, M.W. and T.J.J.o.t.A.C.S. El-Raghy, *Synthesis and characterization of a remarkable ceramic: Ti3SiC2.* 1996. **79**(7): p. 1953-1956.

23.   Jamil, F., H.M. Ali, and M.M.J.J.o.E.S. Janjua, *MXene based advanced materials for thermal energy storage: a recent review.* 2021. **35**: p. 102322.

24.   Chakroborty, S., V. Bharadwaj, and S.K. Sahoo, *Sensing and biosensing with 2D nanosheets beyond graphene*, in *Sensing and Biosensing with Optically Active Nanomaterials*. 2022, Elsevier. p. 119-141.

25.   Wei, Y., et al., *Advances in the synthesis of 2D MXenes.* 2021. **33**(39): p. 2103148.

26.   Anasori, B., M.R. Lukatskaya, and Y.J.N.R.M. Gogotsi, *2D metal carbides and nitrides (MXenes) for energy storage.* 2017. **2**(2): p. 1-17.

27.   Kanoun, M., S. Goumri-Said, and K. Abdullah, *Theoretical study of physical properties and oxygen incorporation effect in nanolaminated ternary carbides 211-MAX phases*, in *Advances in Science and Technology of Mn+ 1AXn Phases*. 2012, Elsevier. p. 177-196.

28.   Hu, M., et al., *Surface functional groups and interlayer water determine the electrochemical capacitance of Ti3C2 T x MXene.* 2018. **12**(4): p. 3578-3586.

29.   Gogotsi, Y. and B.J.A.n. Anasori, *The rise of MXenes*. 2019, ACS Publications. p. 8491-8494.

30.   Mas-Balleste, R., et al., *2D materials: to graphene and beyond.* 2011. **3**(1): p. 20-30.

31.   Novoselov, K.S., et al., *Two-dimensional atomic crystals.* 2005. **102**(30): p. 10451-10453.

32.   Nicolosi, V., et al., *Liquid exfoliation of layered materials.* 2013. **340**(6139): p. 1226419.

33.   Lukatskaya, M.R., et al., *Cation intercalation and high volumetric capacitance of two-dimensional titanium carbide.* 2013. **341**(6153): p. 1502-1505.

34. Ghidiu, M., et al., *Conductive two-dimensional titanium carbide 'clay'with high volumetric capacitance.* 2014. **516**(7529): p. 78-81.

35. Anasori, B. and Û.G. Gogotsi, *2D metal carbides and nitrides (MXenes)*. Vol. 416. 2019: Springer.

36. Hart, J.L., et al., *Control of MXenes' electronic properties through termination and intercalation.* 2019. **10**(1): p. 522.

37. Lin, Z., et al., *Capacitance of Ti3C2Tx MXene in ionic liquid electrolyte.* 2016. **326**: p. 575-579.

38. Rosi, M., F. Iskandar, and M.J.I.J.o.E.S. Abdullah, *Hydrogel-polymer electrolytes based on polyvinyl alcohol and hydroxyethylcellulose for supercapacitor applications.* 2014. **9**(8): p. 4251-4256.

39. Maleski, K., et al., *Size-dependent physical and electrochemical properties of two-dimensional MXene flakes.* 2018. **10**(29): p. 24491-24498.

40. Chae, Y., et al., *An investigation into the factors governing the oxidation of two-dimensional Ti 3 C 2 MXene.* 2019. **11**(17): p. 8387-8393.

41. Cao, M., et al., *Room temperature oxidation of Ti3C2 MXene for supercapacitor electrodes.* 2017. **164**(14): p. A3933.

42. Areef Billah, A., *Investigation of multiferroic and photocatalytic properties of Li intercalated BiFeO3 nanoparticles prepared by ultrasonication.* 2016.

43. Singh, M.K., et al., *Polarized Raman scattering of multiferroic BiFeO3 epitaxial films with rhombohedral R3c symmetry.* 2006. **88**(4).

44. Wang, J., et al., *Epitaxial BiFeO3 multiferroic thin film heterostructures.* 2003. **299**(5613): p. 1719-1722.

45. Ricinschi, D., K.-Y. Yun, and M.J.J.o.P.C.M. Okuyama, *A mechanism for the 150 μC cm− 2 polarization of BiFeO3 films based on first-principles calculations and new structural data.* 2006. **18**(6): p. L97.

46. Fan, Z., et al., *Stable ferroelectric perovskite structure with giant axial ratio and polarization in epitaxial BiFe0. 6Ga0. 4O3 thin films.* 2015. **7**(4): p. 2648-2653.

47. Hatt, A.J., N.A. Spaldin, and C.J.P.R.B. Ederer, *Strain-induced isosymmetric phase transition in BiFeO 3.* 2010. **81**(5): p. 054109.

48. Zeches, R., et al., *A strain-driven morphotropic phase boundary in BiFeO3.* 2009. **326**(5955): p. 977-980.

49. Ji, W., K. Yao, and Y.C.J.P.R.B. Liang, *Evidence of bulk photovoltaic effect and large tensor coefficient in ferroelectric BiFeO 3 thin films.* 2011. **84**(9): p. 094115.

50. Zhao, T., et al., *Electrical control of antiferromagnetic domains in multiferroic BiFeO3 films at room temperature.* 2006. **5**(10): p. 823-829.

51.   Moriya, T.J.P.R.L., *New mechanism of anisotropic superexchange interaction.* 1960. **4**(5): p. 228.

52.   Walker, J., et al., *Robust polarization and strain behavior of sm-modified BiFeO 3 piezoelectric ceramics.* 2015. **62**(1): p. 83-87.

53.   Yuan, G., S.W. Or, and H.L.W.J.J.o.P.D.A.P. Chan, *Structural transformation and ferroelectric–paraelectric phase transition in Bi1– x Lax FeO3 (x= 0–0.25) multiferroic ceramics.* 2007. **40**(4): p. 1196.

54.   Yang, C.-H., et al., *Doping BiFeO 3: approaches and enhanced functionality.* 2012. **14**(46): p. 15953-15962.

55.   Sun, C., et al., *Multiferroic properties of Bi1– xDyxFeO3 (x= 0–0.2) ceramics at various temperatures.* 2012. **72**: p. 160-163.

56.   Levin, I., et al., *Displacive phase transitions and magnetic structures in Nd-substituted BiFeO3.* 2011. **23**(8): p. 2166-2175.

57.   Pradhan, S.J.J.o.M.S.M.i.E., *Influence of iron deficiency on electric and magnetic behavior of Ho intercalated BiFeO 3 electroceramic.* 2013. **24**: p. 1720-1726.

58.   Kumar, M. and K.J.J.o.a.p. Yadav, *Study of room temperature magnetoelectric coupling in Ti substituted bismuth ferrite system.* 2006. **100**(7).

59.   Xu, Q., et al., *The magnetic properties of Bi (Fe0. 95Co0. 05) O3 ceramics.* 2009. **95**(11).

60.   Xu, Q., et al., *The magnetic properties of BiFeO3 and Bi (Fe0. 95Zn0. 05) O3.* 2009. **485**(1-2): p. 13-16.

61.   Cheong, S.-W. and M.J.N.m. Mostovoy, *Multiferroics: a magnetic twist for ferroelectricity.* 2007. **6**(1): p. 13-20.

62.   Zheng, T. and J.J.J.o.M.C.C. Wu, *Enhanced piezoelectric activity in high-temperature Bi 1– x– y Sm x La y FeO 3 lead-free ceramics.* 2015. **3**(15): p. 3684-3693.

63.   Tahir, R., et al., *Emergence of strong room-temperature ferroelectricity and multiferroicity in 2D-Ti $_3$ C $_2$ T $_x$ free-standing MXene film.* 2022.

64.   Tahir, R., et al., *Multiferroic and ferroelectric phases revealed in 2D Ti3C2Tx MXene film for high performance resistive data storage devices.* 2023. **7**(1): p. 7.

65.   Fatima, S., R. Tahir, and S.J.A.P.L. Rizwan, *Ferroelectric-controlled all MXene nonvolatile flexible memory devices for data storage application.* 2023. **123**(1).

66.   Irfan, S., et al., *Enhanced photocatalytic activity of La 3+ and Se 4+ co-intercalated bismuth ferrite nanostructures.* 2017. **5**(22): p. 11143-11151.

67.   Iqbal, M.A., et al., *Ti3C2-MXene/bismuth ferrite nanohybrids for efficient degradation of organic dyes and colorless pollutants.* 2019. **4**(24): p. 20530-20539.

68.   Epp, J., *X-ray diffraction (XRD) techniques for materials characterization*, in *Materials characterization using nondestructive evaluation (NDE) methods*. 2016, Elsevier. p. 81-124.

69.   Mohammed, A. and A. Abdullah. *Scanning electron microscopy (SEM): A review*. in *Proceedings of the 2018 International Conference on Hydraulics and Pneumatics—HERVEX, Băile Govora, Romania*. 2018.

70.   Vandenabeele, P., *Practical Raman spectroscopy: an introduction*. 2013: John Wiley & Sons.

71.   Dodrill, B. and J.R.J.M.m.t.f.m.c. Lindemuth, *Vibrating sample magnetometry.* 2021: p. 15-37.

72.   Niazi, A., P. Poddar, and A.J.C.S.-B.-. Rastogi, *A precision, low-cost vibrating sample magnetometer.* 2000. **79**(1): p. 99-109.

73.   Wang, H., et al., *Enhancement of the electrical properties of MXene Ti3C2 nanosheets by post-treatments of alkalization and calcination.* 2015. **160**: p. 537-540.

74.   Yang, Y., et al., *Structure properties of BiFeO3 films studied by micro-Raman scattering.* 2008. **103**(9).

75.   Verma, R., et al., *Effect of calcination temperature on structural and morphological properties of bismuth ferrite nanoparticles.* 2021. **47**(3): p. 3680-3691.

76.   Sarycheva, A. and Y.J.C.o.M. Gogotsi, *Raman spectroscopy analysis of the structure and surface chemistry of Ti3C2T x MXene.* 2020. **32**(8): p. 3480-3488.

77.   Scott, J.J.I.F., *Models for the frequency dependence of coercive field and the size dependence of remanent polarization in ferroelectric thin films.* 1996. **12**(2-4): p. 71-81.

78.   Hussain, A., et al., *Ferroelectric Sb-intercalated PMN-PT crystal: high electromechanical response with true-remanent polarization and resistive leakage analyses.* 2018. **29**(22): p. 19567-19577.

79.   Mao, Y., et al., *Size-dependences of the dielectric and ferroelectric properties of BaTiO3/polyvinylidene fluoride nanocomposites.* 2010. **108**(1).

80.   Kumar, M. and K.J.J.o.P.C.M. Yadav, *Study of dielectric, magnetic, ferroelectric and magnetoelectric properties in the PbMnxTi1− xO3 system at room temperature.* 2007. **19**(24): p. 242202.

81.   Reddy, V.A., N.P. Pathak, and R.J.S.s.c. Nath, *Enhanced magnetoelectric coupling in transition-metal-intercalated BiFeO3 thin films.* 2013. **171**: p. 40-45.

82.   Nan, C.-W., et al., *Multiferroic magnetoelectric composites: Historical perspective, status, and future directions.* 2008. **103**(3).

83. Gupta, R., et al., *Performance of magnetoelectric PZT/Ni multiferroic system for energy harvesting application.* 2017. **26**(3): p. 035002.

84. Sigov, A., et al., *Leakage currents in ferroelectric thin films.* 2013. **86**(11): p. 1141-1151.

85. Park, M.H., et al., *Study on the size effect in Hf0. 5Zr0. 5O2 films thinner than 8 nm before and after wake-up field cycling.* 2015. **107**(19).

86. Lyu, J., et al., *High polarization, endurance and retention in sub-5 nm Hf 0.5 Zr 0.5 O 2 films.* 2020. **12**(20): p. 11280-11287.

87. Kim, S.J., et al. *Ferroelectric TiN/Hf0. 5Zr0. 5O2/TiN capacitors with low-voltage operation and high reliability for next-generation FRAM applications*. in *2018 IEEE International Memory Workshop (IMW)*. 2018. IEEE.

88. Zubko, P., et al., *Negative capacitance in multidomain ferroelectric superlattices.* 2016. **534**(7608): p. 524-528.

89. Gurkan, Y.Y., E. Kasapbasi, and Z.J.C.e.j. Cinar, *Enhanced solar photocatalytic activity of TiO2 by selenium (IV) ion-doping: Characterization and DFT modeling of the surface.* 2013. **214**: p. 34-44.

90. Li, H., P.J. Sadler, and H.J.J.o.B.C. Sun, *Unexpectedly Strong Binding of a Large Metal Ion (Bi3+) to Human Serum Transferrin (∗).* 1996. **271**(16): p. 9483-9489.

91. Tang, P., et al., *The structural, optical and enhanced magnetic properties of Bi1− xGdxFe1− yMnyO3 nanoparticles synthesized by sol–gel.* 2015. **622**: p. 194-199.

92. Ungar, T., et al., *Microstructure of carbon blacks determined by X-ray diffraction profile analysis.* 2002. **40**(6): p. 929-937.

93. Haumont, R., et al., *Phonon anomalies and the ferroelectric phase transition in multiferroic BiFeO 3.* 2006. **73**(13): p. 132101.

94. Muneeswaran, M. and N.J.J.o.A.P. Giridharan, *Effect of Dy-substitution on the structural, vibrational, and multiferroic properties of BiFeO3 nanoparticles.* 2014. **115**(21).

95. Singh, H. and K.J.C.I. Yadav, *Structural, dielectric, vibrational and magnetic properties of Sm intercalated BiFeO3 multiferroic ceramics prepared by a rapid liquid phase sintering method.* 2015. **41**(8): p. 9285-9295.

96. Melendres, C., et al., *Raman spectroscopy of nanophase TiO2.* 1989. **4**(5): p. 1246-1250.